RESEARCH ARTICLE | AUGUST 08 2025

Numerical treatment of electrical properties in two-phase electrohydrodynamic systems

Bor Zupan ; Rizwan Zahoor ; Saša Bajt ; Božidar Šarler

Physics of Fluids 37, 083353 (2025)
https://doi.org/10.1063/5.0281409

Numerical treatment of electrical properties in two-phase electrohydrodynamic systems

Cite as: Phys. Fluids **37**, 083353 (2025); doi: 10.1063/5.0281409
Submitted: 19 May 2025 · Accepted: 7 July 2025 ·
Published Online: 8 August 2025

Bor Zupan,[1] Rizwan Zahoor,[1] Saša Bajt,[2,3] and Božidar Šarler[1,4,a)]

AFFILIATIONS

[1]Laboratory for Fluid Dynamics and Thermodynamics, Faculty of Mechanical Engineering, University of Ljubljana, Ljubljana, Slovenia
[2]Center for Free-Electron Laser Science CFEL, Deutsches Elektronen-Synchrotron DESY, Hamburg, Germany
[3]The Hamburg Centre for Ultrafast Imaging, Hamburg, Germany
[4]Laboratory for Simulation of Materials and Processes, Institute of Metals and Technology, Ljubljana, Slovenia

[a)]**Author to whom correspondence should be addressed:** bozidar.sarler@fs.uni-lj.si

ABSTRACT

Generation and manipulation of micrometer-sized liquid jets is highly relevant for applications like sample delivery in serial femtosecond crystallography. A promising method combines gas flow focusing with electrospraying but remains underexplored due to numerical limitations regarding high interfacial electric property gradients. This study addresses this challenge by assessing different approaches for electrohydrodynamic (EHD) numerical treatment of two-phase interfaces within the finite volume method and the volume-of-fluid framework. A new geometric mean interpolation technique was developed to address the limitations of high electric conductivity-ratio gas–liquid systems. The technique was related to the established EHD modeling approaches, comprising two electric force implementations and two electric property interpolation methods. Three verification tests involving no flow conditions demonstrated consistent performance of all solvers regarding the electric equations, and they were charge-conservative. Validation on a free boundary problem experiment revealed varying levels of agreement. Results show that the Coulomb-polarization force implementation combined with weighted harmonic mean interpolation provides the most accurate and physically consistent modeling of electric forces at fluid interfaces, followed by the novel geometric mean technique. The model based on the Coulomb-polarization force is applied to simulate electro-flow-focused jets, capturing the complex interplay of hydrodynamic and electrostatic forces in a high-velocity co-flow configuration. While weighted harmonic mean interpolation yields the highest fidelity regarding the electric force magnitude and electric charge position, it fails for extremely low gas conductivities. The proposed geometric mean interpolation provides a stable alternative for simulating EHD two-phase flows, particularly in configurations with large interfacial electric property gradients.

I. INTRODUCTION

Recent experimental advances[1,2] in the generation of micrometer-sized jets through the combined effects of flow focusing and electrospraying, collectively known as electro-flow focusing (EFF), have demonstrated significant potential for producing sub micrometer jets and droplets. This capability is particularly relevant to rapidly evolving fields such as serial femtosecond crystallography[3] and microsatellite propulsion,[4] where extremely fast (>100 m/s), slender (<1 μm) jets with precise control over breakup and stability are required.

While one-dimensional theoretical models have provided valuable insight into the physics of micrometer-scale jets under external forces over the past two decades,[5] they lack the ability to fully capture the complexities of jet dynamics. This limitation has been partially addressed through numerical simulations,[6,7] which have significantly advanced our understanding of both flow-focusing and electrospraying phenomena. These developments now lay the groundwork for the numerical study of more complex microjet systems, including EFF.

Despite the long-standing knowledge of electrohydrodynamic (EHD) systems,[8] their numerical modeling remains an open challenge. In particular, the accurate treatment of electric property discontinuities at fluid interfaces—especially in systems involving strong dielectric contrast or near-vacuum conditions—represents a key hurdle in the reliable simulation of gas–liquid EFF processes. A deeper exploration of numerical methods, both existing and novel, is therefore essential to resolve these challenges and enable predictive modeling of EFF behavior.

In the first numerical simulations of droplets and jets, the boundary element method[9–13] and the finite element method[14–17] have been used by assuming Stokes or inviscid flow, followed by a less common lattice-Boltzmann approach[18] and a meshless approach[19] for the Navier–Stokes flows.

Recently, multiple theoretical EHD models were adapted for simulations, ranging from a strict electrokinetic approach, which includes the full Poisson–Nerst–Planck (PNP) equations, to a macroscopic model, where electrokinetics is reduced to a measurable macroscopic property such as the electrical conductivity. Strict electrokinetic models require the characterization of all molecular species and their properties. A less rigorous approach, which still deals with electrokinetics, is formulated using volumetric charge density. In this approach, the thermal diffusion of ions is usually neglected. Such simplification is justified if the mechanism of electric drift is large enough compared to that of thermal diffusion. If the Debye length is small compared to other relevant lengths, then the model's accuracy is not seriously compromised.[20] The simplest model, the Taylor–Melcher or the Leaky-Dielectric model (LDM), presumes that all charge is concentrated on the free surface while the bulk of the liquid remains neutral. The LDM is justified when the characteristic electrical relaxation time, $t_e \sim \varepsilon/K$, is much shorter than any hydrodynamic time t_h involved, meaning the Ohmic charge migration is presumed to happen instantaneously. Here, ε and K denote the electrical permittivity and electrical conductivity, respectively. The only relevant electrical variable in the LDM is thus the surface charge density σ_E. Using insight provided by Baygets and Saville,[21] a rigorous analysis was done[22–24] to show that the LDM follows from the electrokinetic model after proper simplifications.[20]

Consequently, with different models and theoretical assumptions (e.g., a perfectly conducting or a dielectric fluid pair), various forms of the electric equation and the charge conservation equation were implemented, listed in Table I. Several implementations of the electric force are specified in Table II. In most publications, the Maxwell stress tensor force (MSTF) and the Coulomb and polarization force (CPF) forms of the electric force implementation are considered equivalent (for derivation, see Appendix A).

Symbols in Tables I and II represent the electric field $\boldsymbol{E}$, Faraday's constant F, valence number z, molar concentration n, volumetric charge density ρ_E, electric potential ϕ, fluid velocity $\boldsymbol{u}$, elementary charge e, mobility w, diffusion coefficient D, rate of species production r, the unit vector in the normal direction $\boldsymbol{n}$, the electric force per unit volume $\boldsymbol{F}_E$, the Maxwell stress tensor (MST) $\boldsymbol{\tau}_E$, the identity tensor $\mathbf{I}$, and the electric permittivity of the vacuum $\varepsilon_0 = 8.854 \times 10^{-12}\ \mathrm{Fm}^{-1}$. Operator $||\mathrm{x}||$ denotes the jump of variable x over an interface, and k specifies the chemical species index.

TABLE II. Different forms of the electric force implementation; MSTF, CF, and CPF stand for Maxwell stress tensor force, Coulomb force, and Coulomb and polarization force.

Electric force implementation	
$\boldsymbol{F}_E = \nabla \cdot \boldsymbol{\tau}_E = \nabla \cdot \left(\varepsilon \boldsymbol{E} \otimes \boldsymbol{E} - \frac{1}{2}\varepsilon E^2 \mathbf{I}\right)$	MSTF
$\boldsymbol{F}_E = \rho_E \boldsymbol{E}$	CF
$\boldsymbol{F}_E = \rho_E \boldsymbol{E} - \frac{1}{2}E^2 \nabla \varepsilon$	CPF

The recent widespread adoption of finite volume method (FVM) solvers, often combined with the volume-of-fluid (VOF) approach for interface capturing, has significantly shaped the current landscape of multiphase EHD simulations. As a result, FVM-VOF frameworks have become the dominant choice for simulating such systems. VOF utilizes an additional scalar volume fraction function $\alpha_i = V_i/V$, where index i specifies the phase, and V is the volume of the cell. In cells with the interface, $\alpha_i \in (0, 1)$, the fluid physical properties are corrected appropriately. Standardly, the physical properties are adjusted using the weighted arithmetic mean interpolation (WAM), which we can write for a general property Ψ as $\Psi = \Psi_1\alpha_1 + \Psi_2\alpha_2$. Tomar *et al.*[25] reported that even though WAM is typically used in the VOF method to interpolate the density and viscosity values, weighted harmonic mean interpolation (WHM) should be used when interpolating the electrical properties of fluids. For a general property Ψ, the WHM is defined as $\Psi = 1/(\alpha_1/\Psi_1 + \alpha_2/\Psi_2)$. This claim was later disputed by López-Herrera *et al.*,[6] who concluded that WHM offers no improved accuracy over the WAM for moderately conductive-dielectric fluid pairs.

We highlight the overlooked difference between the WAM and WHM methods: the influence of the relative difference between the interpolated fluid properties. Figure 1 shows the difference between WAM and WHM interpolation of electric conductivity between a moderately conducting pair, with the conductivity ratio λ_K of 10^1, and a conductor-dielectric pair with the conductivity ratio λ_K of 10^6. The conductivity ratio λ_K is determined by dividing the higher conductivity value by the lower conductivity value of the pair. As seen in Fig. 1, the

TABLE I. Different forms of the electric equation and charge conservation.

Electric equation		Conservation of species/free charge	
$\nabla \cdot (\varepsilon \boldsymbol{E}) = -\sum_k F z_k n_k$	PNP	$\frac{\partial n_k}{\partial t} + \nabla \cdot (n_k \boldsymbol{u} + n_k e z_k w_k \boldsymbol{E} - D_k \nabla n_k) = r_k$	PNP
$\nabla \cdot (\varepsilon \boldsymbol{E}) = \rho_E$	Poisson	$\frac{\partial \rho_E}{\partial t} + \nabla \cdot (\rho_E \boldsymbol{u} + K\boldsymbol{E}) = 0$	ρ_E 1
$\nabla^2 \phi = 0$	Laplace	$\frac{\partial \rho_E}{\partial t} + \nabla \cdot (K\boldsymbol{E}) = 0$	ρ_E 2
		$\nabla \cdot (K\boldsymbol{E}) = 0$	LDM
		$\frac{\partial \sigma_E}{\partial t} + \boldsymbol{u} \cdot \nabla_s \sigma_E - \sigma_E \boldsymbol{n} \cdot (\boldsymbol{n} \cdot \nabla) \cdot \boldsymbol{u} + ||K\boldsymbol{E} \cdot \boldsymbol{n}|| = 0$	σ_E

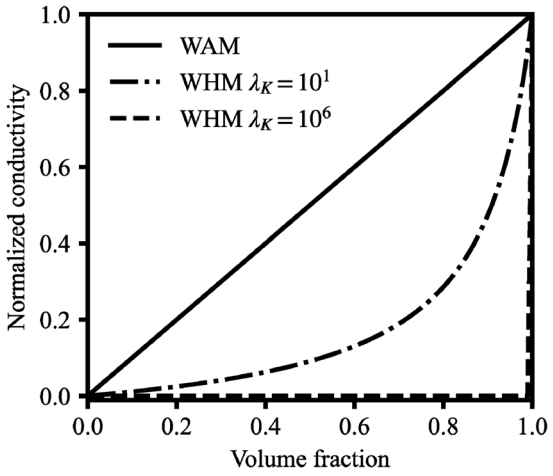

FIG. 1. Interpolation function shape for WAM and WHM between a pair of similarly conducting fluids ($\lambda_K = 10^1$) and a pair with a high conductivity ratio ($\lambda_K = 10^6$). The vertical axis is normalized to the highest conductivity value.

high conductivity ratio between the phases at the interface essentially assigns the lower conductivity value to all cells involving the interface when using WHM. It leads to a very abrupt difference in the physical properties between neighboring cells. For instance, Huh and Wirz[26] recently reported code failure due to abrupt differences while using the WHM scheme at the vacuum-liquid interface. Consequently, they used a weighing power mean (WPM) interpolation scheme, which blends the WAM and WHM methods.

The remarkable diversity of physical phenomena observed in coupled EHD systems, even within a specialized area such as liquid jets, becomes evident when reviewing the publications from the past two decades. Table III presents recent studies on modeling liquid jets in high-voltage fields (e.g., electrospray, Taylor cone formation, steady cone-jet mode, etc.). Abbreviations for the models employed are provided in Tables I and II. Interface tracking methods, aside from the already mentioned volume of fluid (VOF) method, are abbreviated as follows: level set (LS), coupled level set and volume of fluid (CLSVOF), and solution algorithm and volume of fluid (SOLA-VOF). The simplification or derivation of the equations outlined in Tables I and II are not discussed further, as additional details can be found in the provided references.

Fluid dynamic phenomena are typically governed by a dominant force or a ratio of competing forces that dictate the physical response of the system. A notable exception is the production of micrometer-sized jets via electrospray phenomena in the steady cone-jet mode. These systems exhibit high dimensional parameter spaces even in steady or quasi-steady states[27] and a complex interplay of hydrodynamical (viscous, inertial, surface tension) and electrical forces. The primary challenge in numerical modeling is capturing the delicate force balance at the interface, where the equilibrium of the system is determined. As shown in Table III, research in this field is extensive and ongoing.

In this paper, we evaluate different numerical approaches and devise new ones to model multiphase EHD problems successfully using the FVM-VOF framework. By identifying the optimal modeling strategy, we take a step further and present the first numerical simulation of EFF jets. These jets utilize a high-velocity co-flowing gas to additionally focus the Taylor cone jet, which is characteristic of electrosprays. Unlike conventional electrospraying, EFF systems introduce rapid charge and mass convection coupled with steep velocity gradients at the interface, leading to additional numerical instabilities. To date, only liquid–liquid EFF systems have been numerically studied,[28,29] where the velocity ratio between phases is close to unity.[30] In contrast, the velocity ratio for gas–liquid systems can reach up to and over 70.[31–33]

Liquid–liquid systems provide two important simplifications over the gas–liquid system. First, the electric conductivity ratio λ_K for the liquid–liquid systems[28,29] is usually between 10^3 and 10^6, with the lowest conductivity value of around $10^{-12}\,\mathrm{S\,m^{-1}}$, which is easily captured by either the WHM or WAM interpolation method. In dielectric gas–liquid systems, the electrical conductivity is much lower. For gas mixtures like air, which also contains some water vapor, the conductivity on the order of $K \approx 10^{-14}\,\mathrm{S\,m^{-1}}$ is presumed.[34] An increase in conductivity can be expected in the ionized gas regions, for example, near the electro-jet surface. For near or high vacuum conditions, where the Knudsen continuum limit[35] is not yet reached, the conductivity goes virtually to zero, and λ_K effectively approaches infinity.

The second simplification of the liquid–liquid systems over gas–liquid systems is that some free charge will inevitably migrate from the Debye layer into the focusing fluid in fingerlike structures (see, for example, Ref. 36) due to the low conductivity ratio of the phases. If the focusing liquid is conducting, even poorly, the migrated charge will be transported to the negative electrode and discharged. However, when dielectric gas is used, the free charges can migrate only by convection. Combined with the mixing-enhancing vortices of the high-velocity gas (especially at the simulation startup), one is quickly left with a charge-saturated gas domain, leading to code failure and nonphysical phenomena.

The originality of this work lies in a comprehensive analysis of available EHD modeling approaches, the derivation of a novel interpolation method, and its implementation within OpenFOAM. Furthermore, a gas-focused EFF process simulation is presented, along with a discussion on the challenges of simulating gas-focused liquid jets with a high conductivity ratio between the phases.

In the following, we present the outline of this paper: Section II establishes EHD model formulation in terms of fluid flow, electrostatics, and interface treatment. The numerical solver setup is explained in Sec. III. Section IV contains a detailed analysis of verification and validation procedures used to evaluate the different EHD modeling approaches. Six different solvers are evaluated, which combine three different interpolation methods for electric properties and two different electric force implementations. Sections V and VI focus on the application of the EHD solver in the simulation of the EFF jet. A first numerical insight into EFF phenomena is provided, and the challenges regarding high electric property ratios between phases are discussed. In the final section, we summarize the most important findings.

II. MODEL FORMULATION

A. Fluid flow

We consider an incompressible, laminar, Newtonian two-phase flow under the influence of an electric field, considering surface tension and electrical body forces. In general, the material properties of the

TABLE III. Contemporary works on numerical simulations of coupled EHD systems using FVM for liquid jets, bridges, and droplets. N/A is used where information could not be retrieved from the paper. GFM stands for the ghost fluid method.

Year	First author	Electric equation	Charge	Force	Interface	Averaging	Solver
2006	Lastow[37]	Poisson	N/A	CF	VOF	WAM	CFX
2007	Tomar[25]	Laplace	σ_E	CF	CLSVOF	WHM	N/A
2011	López-Herrera[6]	Poisson	ρ_E 1	CPF	VOF	WAM	Gerris
2012	Paknemat[38]	Laplace	LDM	CPF	LS	GFM	N/A
2012	Herrada[39]	Poisson	LDM	CPF	VOF	WHM	Gerris
2013	Berry[40]	Poisson	PNP	CPF	CLSVOF	WHM	N/A
2013	Ferrera[41]	Poisson	ρ_E 2	CPF	VOF	N/A	Gerris
2013	Forget[42]	Poisson	ρ_E 1	CPF	VOF	N/A	OpenFOAM
2013	Najjaran[43]	Poisson	ρ_E 1	CF	VOF	N/A	Fluent
2013	Roghair[44]	Poisson	ρ_E 1	MSTF	VOF	WHM	OpenFOAM
2014	Lima[45]	Poisson	ρ_E 1	CPF	VOF	WAM	OpenFOAM
2015	Chen[46]	Laplace	σ_E	CPF	VOF	WAM	Gerris
2015	López-Herrera[47]	PNP	PNP	CPF	VOF	WAM	Gerris
2015	Roghair[48]	Poisson	ρ_E 1	MSTF	VOF	WHM	OpenFOAM
2016	Rahmanpour[49]	Laplace	ρ_E 1	CF	VOF	N/A	Fluent
2017	Dastourani[50]	Poisson	ρ_E 1	CPF	VOF	N/A	OpenFOAM
2017	Huang[51]	Poisson	ρ_E 1	MSTF	CLSVOF	WHM	OpenFOAM
2017	Rahmanpour[52]	Laplace	ρ_E 1	CF	VOF	N/A	Fluent
2017	Rahmanpour[53]	Poisson	N/A	CPF	SOLA-VOF	N/A	N/A
2017	Wu[54]	Poisson	ρ_E 1	MSTF	VOF	WAM	OpenFOAM
2018	Dastourani[36]	Poisson	ρ_E 1	CPF	VOF	WAM	OpenFOAM
2018	Ghasemi[55]	Poisson	ρ_E 1	CPF	VOF	WAM	Gerris
2019	Guo[56]	Poisson	ρ_E 1	CPF	VOF	N/A	Gerris
2019	Huh[57]	Poisson	ρ_E 1	CPF	VOF	WHM	OpenFOAM
2019	Pan[58]	Poisson	ρ_E 1	CF	VOF	N/A	FLOW-3D
2020	Jiang[59]	Poisson	ρ_E 1	MSTF	VOF	WAM	Fluent
2020	Sahu[60]	Poisson	ρ_E 1	CPF	VOF	WAM	Basilisk
2022	Huh[61]	Poisson	ρ_E 1	CPF	VOF	WPM	OpenFOAM
2022	Huh[26]	Poisson	ρ_E 1	CPF	VOF	WPM	OpenFOAM

phases are assumed to be different. The continuity and momentum equations are posed as

$$\frac{\partial \rho}{\partial t} + \nabla \cdot (\rho \boldsymbol{u}) = 0, \tag{1}$$

$$\frac{\partial (\rho \boldsymbol{u})}{\partial t} + \nabla \cdot (\rho \boldsymbol{u}\boldsymbol{u}) = -\nabla P + \nabla \cdot \left[\mu(\nabla \boldsymbol{u} + \nabla \boldsymbol{u}^T) - \frac{2}{3}\mu(\nabla \cdot \boldsymbol{u})\mathbf{I}\right] + \boldsymbol{F}_{ST} + \boldsymbol{F}_E, \tag{2}$$

where ρ and P represent density and pressure, respectively. Surface tension and the electric force are denoted as $\boldsymbol{F}_{ST}$ and $\boldsymbol{F}_E$ and are given as

$$\boldsymbol{F}_{ST} = \sigma \kappa \nabla \alpha, \tag{3}$$

$$\boldsymbol{F}_E = \nabla \cdot \boldsymbol{\tau}_E = \rho_E E - \frac{1}{2}\boldsymbol{E}^2 \nabla \varepsilon, \tag{4}$$

where σ and κ represent surface tension and curvature, respectively. The two terms on the right-hand side (rhs) of Eq. (4) represent the electric force exerted on free charges in an electric field (Coulombic force) and the polarization force arising from the molecular polarity. These terms are derived directly from the divergence of the MST in the case of electrostatics, as demonstrated in Appendix A. Although theoretically equivalent, the numerical implementations of the electric force (via divergence of the MST or a direct calculation) differ and consequently give different results. This is further discussed in Sec. IV.

B. Electrostatics

The electrostatic model involves Maxwell equations, where the magnetic field can be neglected due to the much longer magnetic characteristic time than the electric one. The relevant governing equations are

$$\nabla \times \boldsymbol{E} = 0, \tag{5}$$

$$\nabla \cdot (\varepsilon \boldsymbol{E}) = \rho_E, \tag{6}$$

where the irrotationality of the electric field allows the electric field to be expressed with the electric potential $\boldsymbol{E} = -\nabla \phi$. The charge conservation equation is derived from the Poisson–Nerst–Planck (PNP) equation,

$$\frac{\partial n_k}{\partial t} + \nabla \cdot (n_k \boldsymbol{u}) = -\nabla \cdot (n_k e z_k w_k \boldsymbol{E}) + \nabla \cdot (D_k \nabla n_k) + r_k, \quad (7)$$

which governs the conservation of k ionic species. Moles of ionic species per unit volume are transformed into charges per unit volume via Avogadro number N_A,

$$\rho_{E,k} = N_A e z_k n_k = F z_k n_k, \quad (8)$$

where the Avogadro number and charge can be merged into the Faraday constant $F = N_A e$. Symbol $\rho_{E,k}$ is the charge density of species k. Summation over all species yields the macroscopic or volumetric charge density, as used in Eqs. (4) and (6)

$$\rho_E = \sum_k \rho_{E,k} = F \sum_k z_k n_k. \quad (9)$$

We can transform the PNP equation into the conservation equation of macroscopic charge density by multiplying both sides with Fz_k and summing over all k species

$$\frac{\partial \rho_E}{\partial t} + \nabla \cdot (\rho_E \boldsymbol{u}) = -\nabla \cdot (K \boldsymbol{E}) + \sum\nolimits_k D_k \nabla^2 \rho_{E,k} + \sum_k F z_k r_k, \quad (10)$$

where we introduced another macroscopic variable, the electrical conductivity K,

$$K = \sum_k w_k F e z_k^2 n_k. \quad (11)$$

Two assumptions are made to derive the charge conservation equation typically employed in EHD simulations: (i) induced ion velocity due to the thermal diffusion being several orders smaller than the mechanism of electric drift and (ii) zero rate of species production. The last two terms in Eq. (10) are thus omitted to produce the final form

$$\frac{\partial \rho_E}{\partial t} + \nabla \cdot (\rho_E \boldsymbol{u}) = -\nabla \cdot (K \boldsymbol{E}). \quad (12)$$

Assumptions limit our model to systems without ongoing reactions producing ionic species and fields of relatively high electric potential. Both simplifications are reasonable in most engineering systems with liquid jets, droplets, and liquid bridges under the influence of electric fields and using common organic solvents. Equation (12) represents the general form of the charge conservation equation in the volumetric charge density approach (see form ρ_E 1 in Tables I and III). It can be further simplified in the case of a dielectric-dielectric or a conducting-conducting fluid pair, but we will use it in its general form as it applies to all cases. The surface charge convection is also neglected, consistent with the assumption of a low electric Reynolds number.[62,63] This simplification is commonly used when charge relaxation occurs much faster than the fluid motion, resulting in negligible convective transport of interfacial charges. While this leads to a more idealized model, it allows for a coherent comparison with analytical solutions and controlled validation cases. The limitations of this assumption are acknowledged, particularly in the experimental context of EFF jets, where solvents with very low conductivity (e.g., hexane) are sometimes used.

C. Interface treatment

We use the FVM,[64] which strictly conserves transported quantities, to transform the partial differential equations into a system of linear algebraic equations. The interface in Eq. (3) is resolved using the VOF[65] method. The VOF method employs an additional interface advection equation to resolve the spatial and temporal evolution of the interface

$$\frac{\partial \alpha}{\partial t} + \nabla \cdot (\alpha \boldsymbol{u}) = 0, \quad (13)$$

where the curvature κ in Eq. (3) is calculated via the continuum surface force model by Brackbill[66]

$$\kappa = -\nabla \cdot \left(\frac{\nabla \alpha}{|\nabla \alpha|} \right). \quad (14)$$

Equation (13) must be accurately solved to maintain a sharp interface, which is not straightforward considering the diffusive nature of the second term. We employ the algebraic VOF method, where a third term is added, which limits the spread of the interface in the normal direction by introducing the compression velocity $\boldsymbol{u}_C$,

$$\frac{\partial \alpha}{\partial t} + \nabla \cdot (\alpha \boldsymbol{u}) + \nabla \cdot (\alpha(1-\alpha)\boldsymbol{u}_C) = 0, \quad (15)$$

$$\boldsymbol{u}_C = C_\alpha \left| \frac{\phi_\alpha}{|S_\alpha|} \right| \boldsymbol{n}, \quad (16)$$

where C_α is the free parameter for adjusting the compression ratio and ϕ_α, S_α, and $\boldsymbol{n}$ are the velocity flux, face surface area, and the interface normal, respectively.

Conventionally, in the VOF method, fluid properties, such as density and viscosity, are interpolated using the WAM. As mentioned in the introduction, there is an ongoing discussion regarding the interpolation method for electrical properties. This discussion is particularly important in the case of EHD microfluidics, as the resulting physical phenomena arise from the intricate interplay of interfacial forces. As Huh and Wirz[26] pointed out, even a slight adjustment in the interpolation method, from a diffusive WAM to a slightly sharper WPM, can in some cases increase the maximum charge density at the interface nearly tenfold. In 2022, Huh and Wirz[26] proposed a new interpolation scheme (WPM), which uses a free parameter f,

$$\Psi = \left(\alpha_1 \Psi_1^{1/f} + \alpha_2 \Psi_2^{1/f} \right)^f. \quad (17)$$

At $f = 1$ and $f = -1$, Eq. (17) reduces to WAM and WHM, respectively, while at $f > 1$ it provides a blend. They reported a sharper variation of ε and K with less false diffusion with a larger f, but concluded no further significant dependence on f for $f > 20$. Such behavior suggests that WPM approaches a limit at $f \to \infty$, which would be the optimal blending function according to their results.

We can derive the limit $f \to \infty$ of Eq. (17) by considering

$$\ln(\Psi) = f \cdot \ln\left(\alpha_1 \Psi_1^{1/f} + \alpha_2 \Psi_2^{1/f} \right). \quad (18)$$

Here, we note that terms with the power of $1/f$ approach 1 as f approaches infinity, and we can use the first-order approximation for small powers

$$\Psi^{1/f} \approx 1 + \frac{\ln(\Psi)}{f}, \quad (19)$$

to expand the logarithmic term

$$\ln(\Psi) \approx f \cdot \ln\left(\alpha_1\left(1+\frac{\ln(\Psi_1)}{f}\right)+\alpha_2\left(1+\frac{\ln(\Psi_2)}{f}\right)\right). \quad (20)$$

We can simplify Eq. (20) by collecting similar terms and applying $\alpha_1 + \alpha_2 = 1$

$$\ln(\Psi) \approx f \cdot \ln\left(1+\frac{\alpha_1 ln(\Psi_1)+\alpha_2 ln(\Psi_2)}{f}\right). \quad (21)$$

For logarithm $\ln(1+x)$ where $x \ll 1$, a first-order Taylor expansion $\ln(1+x) \approx x$ can be used for approximation

$$\ln(\Psi) \approx \alpha_1 \ln(\Psi_1) + \alpha_2 \ln(\Psi_2), \quad (22)$$

from which the sought limit can be recovered by exponentiation

$$\Psi \approx \Psi_1^{\alpha_1}\Psi_2^{\alpha_2}. \quad (23)$$

Derived function $\Psi = \Psi_1^{\alpha_1}\Psi_2^{\alpha_2}$, also called the geometric mean (GM), follows directly from the WPM when $f \to \infty$. We compare it to WAM and WHM to find a favorable interpolation method for electrical properties with the VOF method for coupled EHD simulations.

III. NUMERICAL METHOD

We utilized the open-source software OpenFOAM,[67] which provides a FVM implementation of a wide range of physical models and solvers. Specifically, we adapted the *interFoam* solver (version v2312), which employs the algebraic VOF method. To compute the electric force—Eq. (4), we solved the Poisson equation—Eq. (6), and the conservation of charge equation—Eq. (12). For clarity, all numerically implemented equations are collected in Appendix B. In the present model, the permittivity and conductivity are treated as continuous fields by blending the phase values using the volume fraction, which enables the computation of its gradient within the finite volume framework despite the physical discontinuity at the interface.

Partial differential equations were solved using the PIMPLE algorithm, a hybrid of the PISO (Pressure Implicit with Splitting of Operators) and SIMPLE (Semi-Implicit Method for Pressure-linked Equations) algorithms. An adaptive time stepping approach ensured stability with a global Courant number $\mathrm{Co} = 0.25$. Algebraic equations were solved using the preconditioned conjugate gradient (PCG) solver and the diagonal incomplete Cholesky (DIC) solver. For the volumetric charge density, the algebraic equations were preconditioned using diagonal incomplete LU decomposition (DILU) and solved using the preconditioned bi-conjugate gradient solver (PBiCG), which are often used together where non-symmetric systems arise. All cases were computed on a 16-core AMD Ryzen 9 7950X processor.

IV. NUMERICAL MODEL VERIFICATION AND VALIDATION

This section presents a comparative analysis of six different solvers. Solvers vary in their implementation of the electric force (either MSTF or CPF) and their choice of the interpolation method (WAM, WHM, or GM). They are compared on three standard benchmark verification tests and validated on the well-documented droplet deformation test against analytical solutions and experiments.

A. Verification tests

To verify the implementation of Eqs. (6) and (12), we calculated three cases introduced in the 2011 paper by López-Herrera *et al.*:[6] the planar layer test, the conducting cylinder test, and the Gaussian charge bump relaxation test. The setup and boundary conditions of the test are shown in Fig. 2.

The domain was discretized using a uniform structured Cartesian mesh. The resolution of the mesh is denoted by λ, which specifies the number of cells in x and y directions as 2^{λ}. The total number of cells is then $2^{2\lambda}$.

1. Planar layer test

In the *planar layer test*, see Fig. 2(a), two fluids with different electrical properties are stacked vertically and share a stable interface. An electric potential difference is generated between the top and bottom boundary (ϕ_0 is the non-zero specified potential, H is the arbitrary height), which induces an electric field through the domain. Three fluid pairs encapsulating the boundary cases are simulated: conductive-conductive, dielectric-dielectric, and conductive-dielectric. The induced electric field and pressure difference over the interface are compared with the dimensionless analytical solutions for MSTF and CPF implementations of the electric force in Table V. The setup and analytical solutions are specified in Table IV.

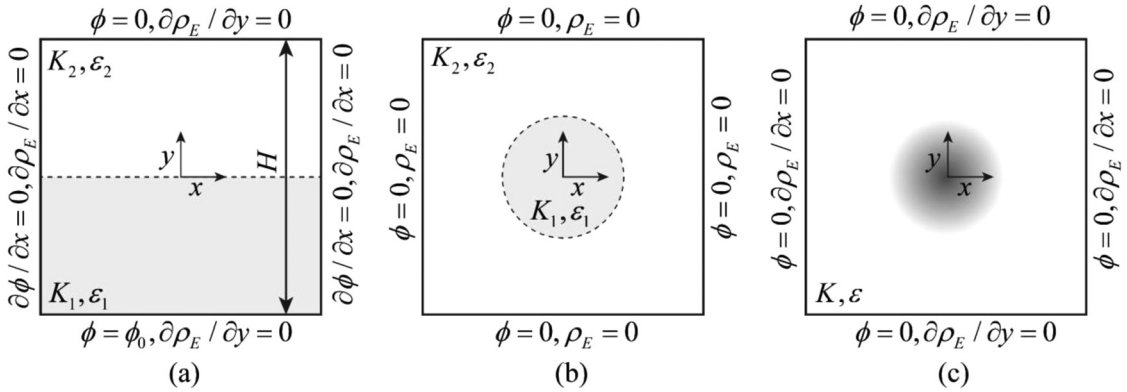

FIG. 2. Verification tests setup: (a) planar layer test, (b) conducting cylinder test, and (c) Gaussian charge bump relaxation test.

TABLE IV. Dimensionless parameters and dimensionless analytical solutions for the three cases. Electric potential, length, and pressure jump are scaled with ϕ_0, H, and $\varepsilon_2\phi_0^2/H^2$, respectively. Analytical solutions are adapted after López-Herrera *et al.*[6]

Fluid pair	$\varepsilon_1/\varepsilon_2$	K_1/K_2	$\lvert E_1\rvert^{an}$	$\lvert E_2\rvert^{an}$	ΔP^{an}
Conductive–dielectric	…	…	0	2	-2
Dielectric–dielectric	3	…	$\frac{2}{1+\beta}$	$\frac{2\beta}{1+\beta}$	$-\frac{2\beta(\beta-1)}{(1+\beta)^2}$
Conductive–conductive	2	0.25	$\frac{2}{1+\eta}$	$\frac{2\eta}{1+\eta}$	$-\frac{2(\eta^2-\beta)}{(1+\eta)^2}$

The solution of the electric field converges toward its analytical value at higher grid resolution and is independent of the electric force implementation. This is to be expected since the Poisson equation governs the electric field, Eq. (6). Interestingly, the calculation of the pressure jump over the interface (ΔP) using direct calculation of the electric force (CPF) converges to a different value than the conservative divergence form (MSTF). The magnitude of the erroneous limit depends on the specific case and arises from the inaccurate estimation of the polarization term, as noticed also by Welch and Biswas.[68] In the case of the electric permittivity on the order of $10^{-12}\,\mathrm{F\,m^{-1}}$, which is usual for common solvents, gasses, air, and the vacuum, the error in pressure calculation is also of the same order, which shows that the use of the CPF does not seriously compromise the solution.

In all cases, a first-order spatial convergence is achieved since the errors halved with the doubling of grid resolution. Interestingly, the pressure jump error is roughly the sum of the electric field errors in the MSTF method. This indicates that the conservative nature of the MST enables a conservative calculation of electrical stresses in each grid cell. The selection of the interpolation method did not influence the results, with changes below 0.5%. Results in Table V were calculated using the WHM interpolation.

2. Conducting cylinder test

In the *conducting cylinder test*, see Fig. 2(b), a conducting cylinder of radius R (fluid 1) is placed in the center of a dielectric domain (fluid 2). Uniform charge distribution $\rho_{E,0}$ is prescribed inside the cylinder at time zero and is repelled toward the interface as time progresses. A discrete jump in the magnitude of the electric field $|\boldsymbol{E}|$ is expected at the interface since the conducting cylinder is at the same electric potential, and the permittivity of the surrounding fluid governs the potential drop outside $r \geq R$, where r is the radial position. The analytical solution[6] of the electric field magnitude is

$$|\boldsymbol{E}|(r) = \begin{cases} 0 & \text{for } r < R, \\ \dfrac{Q}{2\pi\varepsilon_2} r^{-1} & \text{for } r \geq R, \end{cases} \tag{24}$$

where $Q = \pi R^2 \rho_{E,0}$ is the total charge per unit cylinder. Test parameters were the following: $K_1 = 3\,\mathrm{S\,m^{-1}}$, $\varepsilon_1 = 3\,\mathrm{F\,m^{-1}}$, $K_2 = 0\,\mathrm{S\,m^{-1}}$, $\varepsilon_2 = 2\,\mathrm{F\,m^{-1}}$, $\rho_{E,0} = 0.5\,\mathrm{C\,m^{-3}}$, and $R = 0.05\,\mathrm{m}$ (domain is $1 \times 1\,\mathrm{m}$). Four grid resolutions were tested, with λ in the range of 6–9.

The solution of Eq. (24) is compared with numerical results in Fig. 3(a). The numerical solution converges toward the analytical limit with increasing grid resolution. Furthermore, the total charge within the domain is conserved, regardless of grid resolution, as shown in Fig. 3(b). The total charge also converges to the analytical solution with higher grid resolution. This was anticipated since the area of the cylinder's cross section approaches theoretical value as the interface becomes more refined. The selection of the interpolation method or electric force implementation did not influence the results. Results in Figs. 3(a) and 3(b) were calculated using the CPF-WHM solver.

TABLE V. Comparison between numerical results and analytical solutions for the planar layer test. Four grid resolutions were tested, where the grid number specifies the number of cells in the direction normal to the interface. Errors were calculated as $X^{err} = 1 - X^{num}/X^{an}$ (%), where $X \in (|E_1|, |E_2|, \Delta P)$. Two implementations of the electric force are compared in consecutive columns for each variable X. In the conductive-dielectric pair, the value of $|E_1|$ is always smaller than 1×10^{-12}, corresponding to the approximate zero value.

	$\lvert E_1\rvert$ Error (%)		$\lvert E_2\rvert$ Error (%)		ΔP Error (%)	
λ	CPF	MSTF	CPF	MSTF	CPF	MSTF
Conductive–dielectric pair						
5	0	0	3.05	3.22	33.00	6.57
6	0	0	1.65	1.60	29.00	3.22
7	0	0	0.65	0.80	26.50	1.65
8	0	0	0.35	0.40	26.00	0.90
Dielectric–dielectric pair						
5	0.80	0.80	0.80	0.80	12.16	1.59
6	0.40	0.40	0.40	0.40	11.28	0.79
7	0.20	0.20	0.20	0.20	10.85	0.39
8	0.00	0.00	0.07	0.07	10.64	0.20
Conductive–conductive pair						
5	1.13	1.13	1.25	1.25	0.24	2.30
6	0.56	0.56	0.50	0.50	1.37	1.13
7	0.31	0.31	0.25	0.25	1.94	0.56
8	0.12	0.12	0.12	0.12	2.18	0.28

3. Gaussian charge bump relaxation test

Conservation of charge implementation is further verified in the *Gaussian charge bump relaxation test*, as seen in Fig. 2(c). The setup is the following: consider a two-dimensional Gaussian charge bump centered in a square domain (size $1 \times 1\,\mathrm{m}$, $\lambda = 8$) consisting of a single, conducting liquid with $K = 1\,\mathrm{S\,m^{-1}}$ and $\varepsilon = 2\,\mathrm{F\,m^{-1}}$. The initial charge density profile is set according to

$$\rho_E(\boldsymbol{p}, t_0) = \frac{1}{a\sqrt{2\pi}} e^{\frac{r^2}{2a^2}}, \tag{25}$$

where $\boldsymbol{p} = (x, y)$ is the position vector, t_0 is time zero, $r = \sqrt{x^2 + y^2}$ is the radius vector from the domain center, and $a = 0.05$ is a constant. As time proceeds, the charge bump decays exponentially following the analytical solution:[6]

$$\rho_E(\boldsymbol{p}, t) = \rho_E(\boldsymbol{p}, t_0) e^{-\frac{K}{\varepsilon}t}. \tag{26}$$

A comparison between the analytical and numerical solutions is presented in Fig. 3(c), where the volumetric charge density distribution is

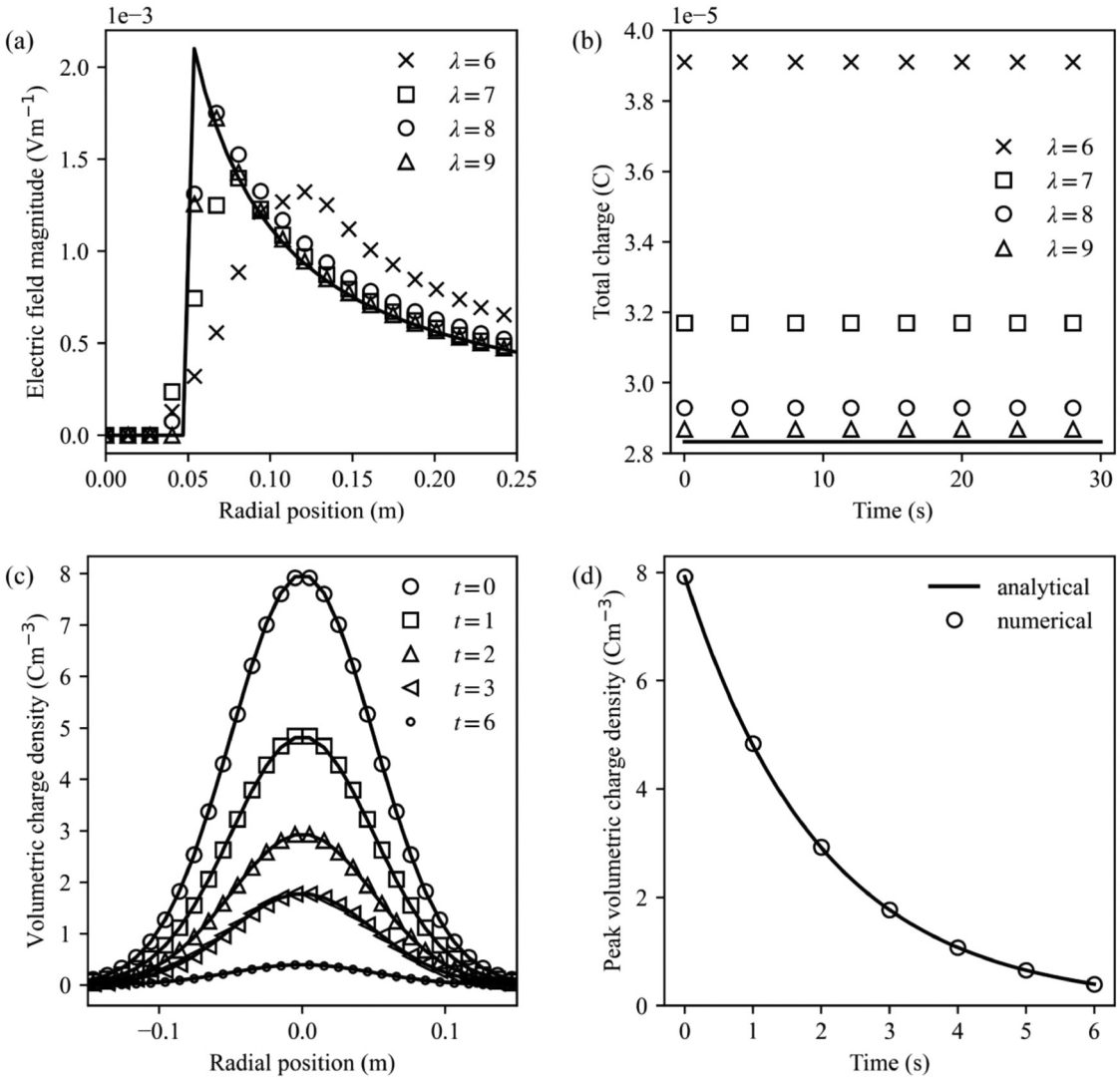

FIG. 3. Verification tests: (a) electric field magnitude for the charged cylinder test, (b) total charge in the computational domain for the charged cylinder case, (c) volumetric charge density distribution for the Gaussian charge bump test, and (d) the decay of the peak volumetric charge density. Time in (c) is in seconds. The analytical solution is drawn with a solid black line.

sampled radially at five different time steps and compared to Eq. (26). Further comparison is shown in Fig. 3(d), where the time decay of the peak charge density, located at the center of the domain, is sampled over multiple time steps and compared with the analytical results. Both tests exhibit an exact match with the analytical predictions, validating the implementation of the charge transport equation. Likewise, in the conducting cylinder test, no influence of solver selection on the result was noted. This is expected since we solve only the electric equations in a computational domain without an interface. Results in Figs. 3(c) and 3(d) were calculated using the CPF-WHM solver.

Verification tests confirm the charge-conservative nature of the proposed solvers and the implementation of the electric equations. However, they provide limited insight into the influence of the electric force implementation and show no variation in the results based on the interpolation method of electric properties.

B. Experimental validation

Validation was performed on the well-studied test of droplet deformation in an electric field, with results compared against two analytical models, the linear model by Taylor[8] and the later improved nonlinear model by Ajayi,[69] two experimental data sets taken from the 2000 paper by Ha ∼and Yang,[70] and the 2024 paper by Karp *et al.*[71]

1. Test setup

The numerical setup for the Ha and Yang[70] paper [see Fig. 4(a) left] includes a droplet with an initial radius r and rheological

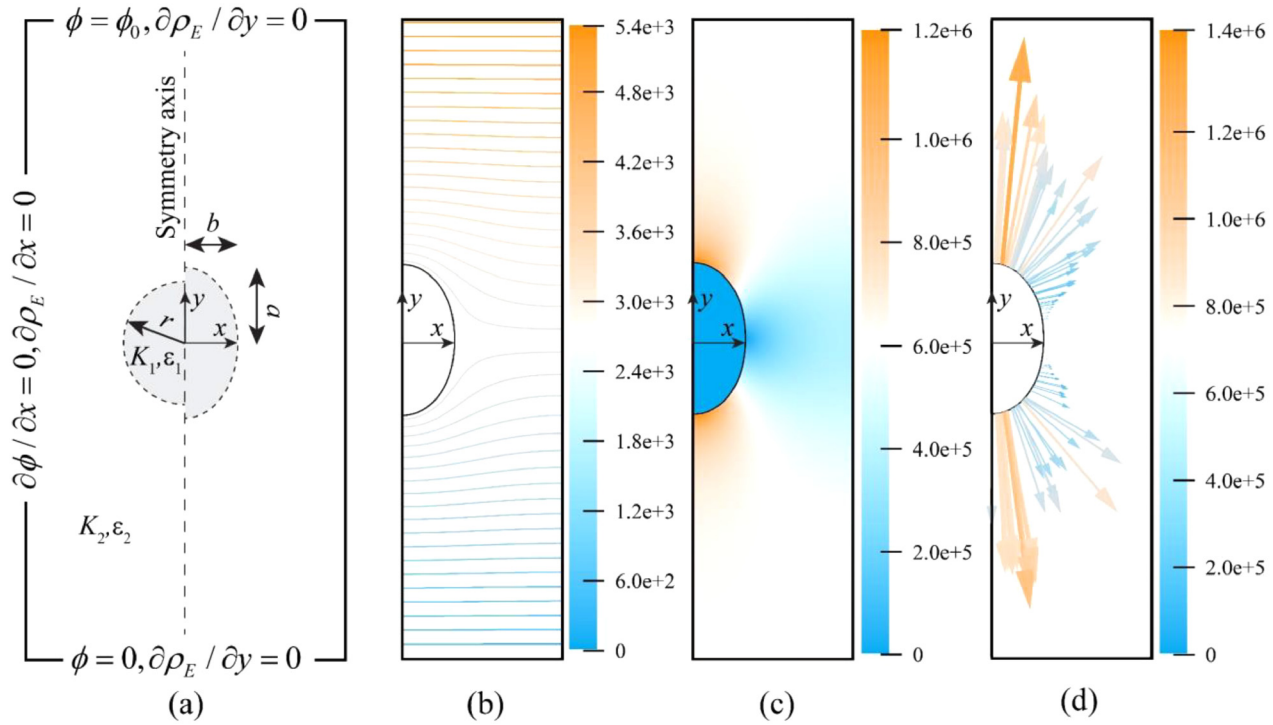

FIG. 4. A steady-state solution of droplet deformation: (a) initial and boundary conditions (left) and the deformed droplet with attributing dimensions (right), with the steady-state solutions of the (b) electric potential in volts, (c) electric field magnitude in volts per meter, and (d) the electric force at the surface in newtons per cubic meter. Results in (b)–(d) were calculated with the CPF-WHM solver and $Ca_E = 0.2$.

properties μ_1, K_1, and ε_1 which was placed at the center of a two-dimensional computational domain of size $2.5\,r \times 10\,r$. The buoyancy effects were ignored by using the same external fluid density as the droplet. However, the rheological properties of the external fluid were described with μ_2, K_2, and ε_2. An electric field of strength E_0 was applied in the vertical direction, which deformed the droplet. A deformation parameter

$$D = \frac{a-b}{a+b} \tag{27}$$

was calculated from the droplet's major and minor axis stretch [see Fig. 4(a) right] together with the electric capillary number Ca_E, which varied between 0.01 and 0.2

$$Ca_E = \frac{\varepsilon_2 E_0^2 r}{\sigma}. \tag{28}$$

Other dimensionless numbers associated with the problem are the electric conductivity ratio $R = K_1/K_2$, the electric permittivity ratio $S = \varepsilon_1/\varepsilon_2$ and the dynamic viscosity ratio $M = \mu_1/\mu_2$, which equaled $R = 10^{-8}$, $S = 36.36$ and $M = 0.1$ for all calculated cases with surface tension $\sigma = 0.028\,\mathrm{N\,m^{-1}}$ and density $\rho = 1000\,\mathrm{kg\,m^{-3}}$.

A uniform, structured Cartesian mesh was employed, and a mesh sensitivity study was performed using resolutions of 40, 60, 80, and 100 cells across the radius of the droplet. Therefore, the largest and the smallest cell sizes correspond to 25 and 10 μm, respectively. The results in Fig. 5 indicate that the final droplet deformation remained consistent between the cases with 80 and 100 cells. Consequently, a mesh resolution of 80 cells across the droplet radius was adopted.

When a steady state solution is reached, a flow field shown in Fig. 6 arises. Two characteristic recirculation zones develop, the first in

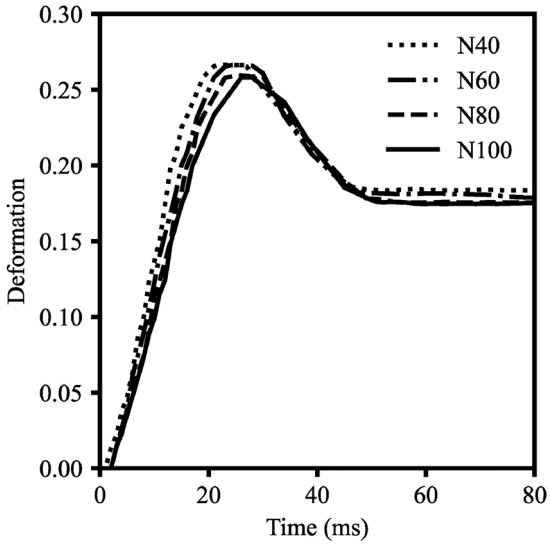

FIG. 5. Mesh sensitivity study with N specifying the number of cells across the droplet radius. CPF-WHM solver was used with $Ca_E = 0.2$.

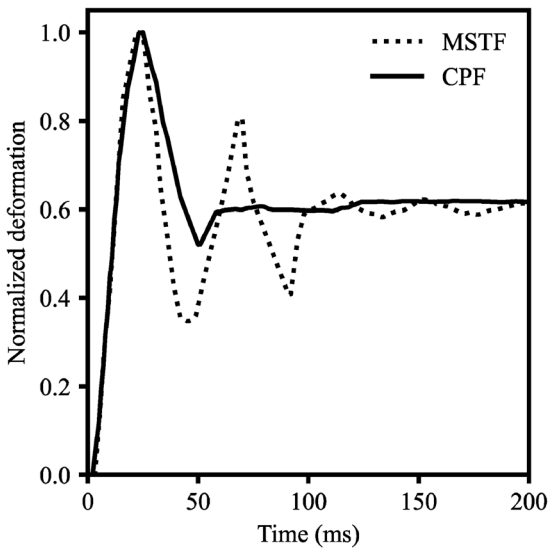

FIG. 6. Comparison of the deformation oscillations in the transient stage between MSTF and CPF with $Ca_E = 0.16$. Both plots are normalized to the maximum deformation value. WHM interpolation was used in both cases. The MSTF continues to oscillate further than 200 ms, settling at the same normalized deformation as CPF.

the droplet and the second in the surrounding medium, driven by the shear forces at the interface.

2. Electric force implementation comparison

A normalized plot of the deformation is shown in Fig. 7. The plot reveals distinct differences in the performance of the two electric force implementations. Suppose the deformation is not normalized (see Fig. 8). In that case, the MSTF implementation predicts only half the steady-state deformation compared to CPF, indicating a significant underestimation of the droplet's deformation. Furthermore, the MSTF implementation exhibits prolonged and high-amplitude oscillations during the transient phase, suggesting less numerical damping and potentially reduced stability. In contrast, the CPF implementation demonstrates a more stable and physically consistent behavior with rapid damping of oscillations and smooth convergence to the steady-state value. Interestingly, despite the differences in transient behavior and final deformation, both implementations ultimately converge to a similar normalized steady-state deformation, which is around 60% of the maximum deformation.

The difference in steady-state deformation is traced to variations in the peak volumetric charge density predicted by the MSTF and CPF solvers. This disparity results in the peak charge density for the CPF solver being up to 68% higher than that of the MSTF solver. The higher peak charge density in CPF contributes to stronger electric forces at the interface (300% increase over MSTF), thereby contributing to the more significant steady-state deformation.

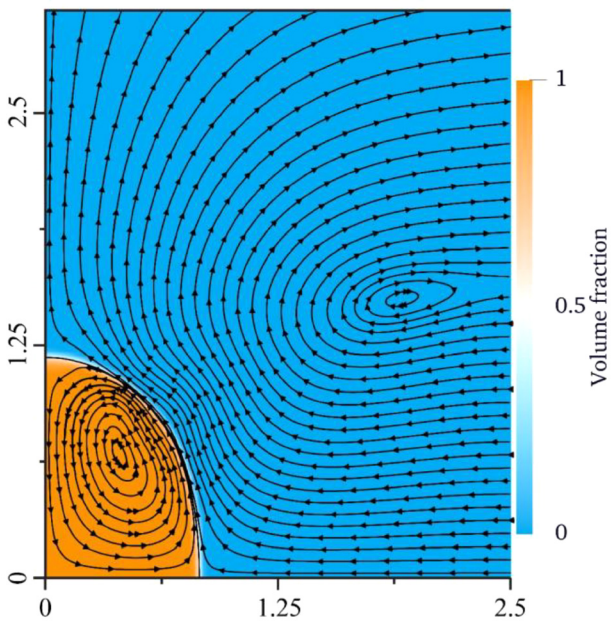

FIG. 7. Streamlines of the flow field in the droplet deformation study, calculated with the CPF-WHM solver, with $Ca_E = 0.20$. Scale is in millimeters.

3. Interpolation functions comparison

As shown in Fig. 8, the choice of interpolation method significantly affects the results when the CPF force implementation is employed. WHM interpolation predicts the highest deformation among the tested methods, closely aligning with experimental data.[70] This alignment is particularly noticeable at higher electric capillary numbers ($Ca_E > 0.1$), where WHM captures the steep increase in deformation observed experimentally. In contrast, both WAM and GM interpolations consistently underestimate deformation by ~10%–15%. Therefore, validation tests employing only the analytical models should be limited to $Ca_E < 0.05$. Experimental validation is crucial for verifying numerical models that capture high deformations.

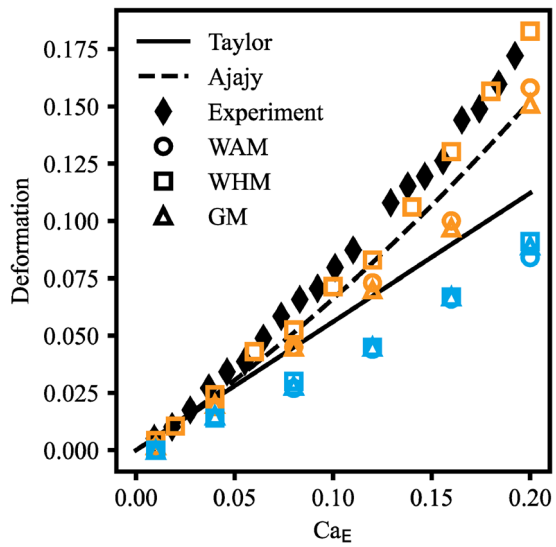

FIG. 8. Interpolation function comparison for the MSTF (blue markers) and CPF (orange markers) solvers. Experimental data are from Ha and Yang[70] and analytical solutions from Taylor[8] and Ajayi.[69]

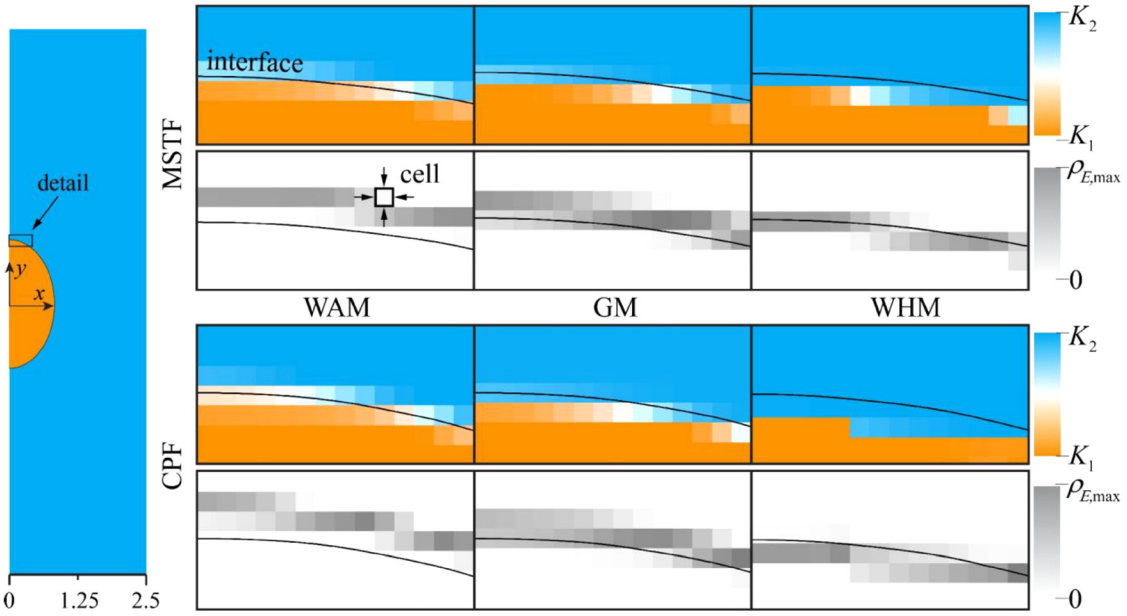

FIG. 9. Electric conductivity K and volumetric charge density ρ_E fields for different interpolation functions and electric force implementations imaged in detail marked on the left. $K_1 = 1 \times 10^{-4}$, $K_2 = 1 \times 10^{-12}$, and $\rho_{E,\max} = 1.96\,\mathrm{C\,m^{-3}}$. Black lines mark the interface ($\alpha = 0.5$) with $\mathrm{Ca_E} = 0.2$ and mesh resolution of 80 for all cases. The size of the detail is $175 \times 87.5\mu$m. Scale on the left is in millimeters. The imaged section was chosen at the area where the strongest electric force is located [see Fig. 4(d)].

For the MSTF force implementation, the interpolation method has no observable impact on droplet deformation. Under these conditions, the deformation exhibits a roughly linear trend with increasing electric capillary number, as shown by the overlapping results of all interpolation methods. Such linear behavior agrees with experimental data only at very low deformation levels ($D < 0.05$), where Taylor's linear model is conventionally applied.[8] Beyond this range, experimental data[70] and predictions from the improved Ajayi's model[69] indicate a nonlinear increase in deformation, which is not captured by the MST implementation.

Figure 9 illustrates the interpolation of electric properties across the fluid interface and their influence on the location of the volumetric charge relative to the computed interface. As anticipated (see Fig. 10), the WHM interpolation results in the most abrupt transitions in electric properties, while GM and WAM produce increasingly smoothed variations. Concerning the interface position, WHM assigns the properties of the outer fluid across the entire interface and even within the droplet. This occurs because even a slight decrease in the volume fraction parameter triggers a sharp change in electric properties.

Although this behavior may initially appear inconsistent, WHM most accurately computes the volumetric charge density at the interface where it physically resides. A similar accuracy is achieved by the GM interpolation method. WAM, which incorporates gradual transitions in fluid properties across the interface, primarily calculates the charge distribution within the outer medium. Consequently, WHM yields electric forces in agreement with experimental data and provides the most physically accurate volumetric charge distribution, which is also captured by the GM method.

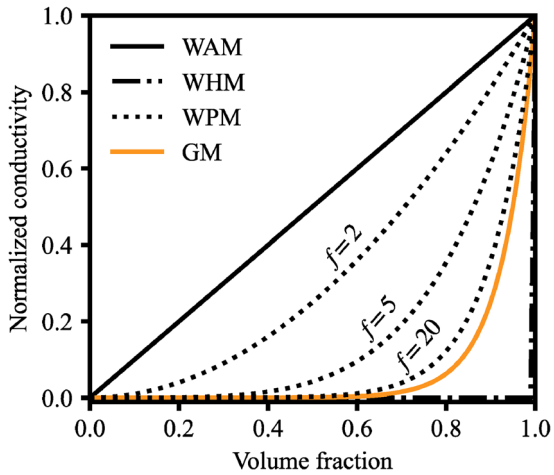

FIG. 10. Comparison of different interpolation functions for $\lambda_K = 10^6$. The WPM method is plotted for the case of f equal 2, 5, and 20. At the $f \to \infty$ limit, the WPM approaches the GM.

4. The velocity field inside the droplet

The validation of the velocity field inside the droplet was performed on a recent experimental dataset by Karp *et al.*,[71] which employed particle image velocimetry. The numerical setup is analogous to the case described at the start of the section, with the following differences. The computational domain size was $6r \times 3r$, with r

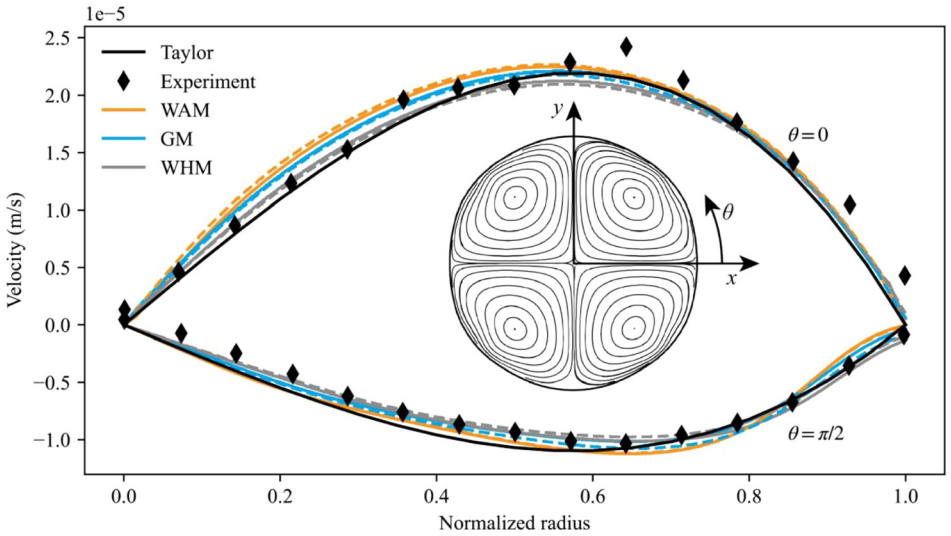

FIG. 11. Radial velocity shown against the normalized radius at two polar angles, $\theta = 0$ and $\theta = \pi/2$. Solid and dashed colored lines represent the CPF and MSTF solver, respectively. The black line represents the analytical solution by Taylor,[8] while the experimental data from Karp *et al.*[71] are marked with diamonds. The inset illustrates the recirculation pattern inside the droplet.

$= 2.25$ mm. Dimensionless numbers were $R = 0.029$, $S = 0.68$, and $M = 0.735$ for all calculated cases with $\sigma = 0.004\,\mathrm{N\,m^{-1}}$. The density ratio of used liquids in the experiment was 1.009 and was set to unity in the simulations. The same number of cells per initial droplet diameter was used.

In addition to the experiment, the results were also compared to the analytical solution provided by Taylor,[8] since the droplet deformation D was below 0.05. The radial component of the velocity vector is calculated from the Cartesian coordinates as $\boldsymbol{u}_r = \boldsymbol{u} \cdot (\cos\theta,\ \sin\theta)$, where θ is the polar angle of the position vector measured from the x axis.

Figure 11 shows the comparison between the experimental, numerical and analytical solutions of the second case from the experimental dataset,[71] with $E_0 = 0.50\,\mathrm{kV/m}$ applied in the positive x direction. The difference between the CPF (solid lines) and the MSTF (dashed lines) solver is negligible, due to the low deformation rate. The interpolation functions influence both the magnitude and the shape of the velocity profile with the WHM method consistently yielding the best agreement with experimental data across both directions, followed by the GM method.

V. ELECTRO-FLOW-FOCUSING SETUP

An axisymmetric domain mimicking the original EFF experimental device by Gañán-Calvo *et al.*[72] was constructed numerically and is shown in Fig. 12. A charged capillary of diameter $D = 100\,\mu$m was placed inside a pressurized metal cylinder (electrode) at zero electric potential, with an orifice of diameter $d = 50\,\mu$m inline with the capillary. The distance between the capillary and the orifice was $H = 100\,\mu$m. The dimensions of the outlet chamber were 1.575×0.5 mm, and the capillary length-to-radius ratio was 6 to ensure the development of the velocity profile. Heptane and air were chosen as the focused and focusing fluids with their properties listed in Table VI. The process parameters were kept constant in all cases with the liquid flow rate Q at $0.75\,\mathrm{ml\,h^{-1}}$, gas overpressure ΔP_g at 20 mbar, and electric potential ϕ_0 at 2 kV. The overpressure was chosen so that the gas remained in the incompressible regime throughout the computational domain (Ma < 0.3, where Ma is the Mach number).

The mesh resolution was chosen based on the mesh independence study, where meshes with the finest resolution of 1.25, 0.63, 0.31, and 0.16 μm were tested. The difference in the jet diameter at the electrode orifice between the 0.31 and 0.16 μm mesh was negligible. Therefore, an axisymmetric structured hexahedral mesh with five levels of local refinement was employed (see Fig. 12). Cells at the finest refinement level were $0.31 \times 0.31\,\mu$m, with a total cell count of ∼140 000. All cases were first calculated on the 0.63 μm mesh with the WAM interpolation until a quasi-steady state solution was obtained (1 ms) to shorten the simulation time and ensure a numerically stable initial solution. After that, the computed fields were mapped onto the finer mesh, and the intended interpolation method was employed. The fluid properties were constant for all cases except for the WHM interpolation, where the conductivity of air was chosen as $K = 1\mathrm{E}^{-12}\,\mathrm{S\,m^{-1}}$, to prevent code failure. The rheological and electrical properties of heptane and air are listed in Table VI, and the boundary conditions are listed in Table VII.

The geometry and process parameters were chosen to ensure the combined effect of the electric and hydrodynamical focusing force.[72] Specifically, the similarity in distances $D \sim L_t \sim H$ and the ratio between the electric to mechanical stress exerted on the jet[72]

$$\chi = \left(\frac{\rho_1 \sigma^2 K_1^2}{\varepsilon_0^2 \Delta P_g^3}\right)^{\frac{1}{3}}, \tag{29}$$

which equals 0.72 in our case. $L_t \sim Q\left(K_1 \rho_1^2 \varepsilon_0^{-1} \sigma^{-1}\right)^{1/3}$ is the transition length or the length where the electric force exerts maximum influence.[72]

VI. RESULTS AND DISCUSSION

For the aforementioned EFF case, we tested the high conductivity ratios with all three interpolations methods. We found that while the WAM and GM are robust for any conductivity ratio, the WHM is stable until the lowest conductivity is roughly $10^{-12}\,\mathrm{S\,m^{-1}}$. However, the conductivity of the gas does not have a significant influence on the jet dynamics except charge conduction from the interface. Once a

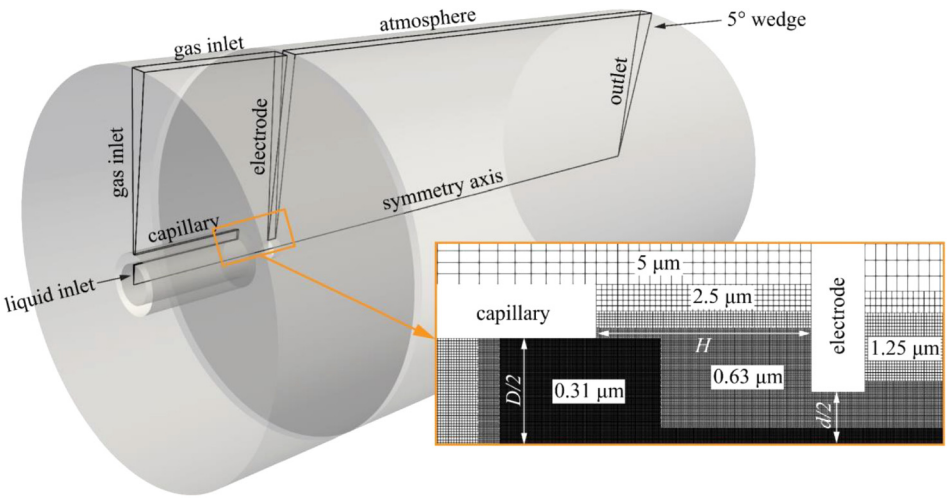

FIG. 12. Computational domains of EFF and mesh refinement detail. Cell dimension in different refinement areas is provided in the zoomed-in region. The device dimensions are: $D = 100\ \mu$m, $d = 50\ \mu$m, and $H = 100\ \mu$m.

TABLE VI. Rheological and electrical properties of heptane and air used in the EFF simulation.

Fluid	$\rho\,(\mathrm{kg\,m^{-3}})$	$\nu\,(\mathrm{m^2\,s^{-1}})$	$K\,(\mathrm{S\,m^{-1}})$	ε_r	$\sigma\,(\mathrm{N\,m^{-1}})$
Heptane	684	5.5×10^{-7}	1×10^{-6}	1.93	0.0186
Air	1.2	1.5×10^{-5}	1×10^{-14}[a]	1	⋯

[a]The electric conductivity of air was set to $1 \times 10^{-12}\,\mathrm{S\,m^{-1}}$ for cases with the WHM interpolation.

quasi-steady state solution is computed, the electric permittivity of the gas could be lowered from 10^{-12} to 10^{-50} with the WAM and GM interpolation, and the difference in jet diameter, jet velocity, or charge density becomes negligible.

Interestingly, the velocity and pressure field results were independent of the interpolation methods but Fig. 13 shows the results obtained with the WAM interpolation. The highest observed velocity was 90 m/s, which occurred in the early transition regime and then lowered to 63 m/s in the quasi-steady state jetting regime. These values justify use of a non-compressible solver and correspond to Mach numbers of 0.265 and 0.185, respectively.

Electric force and electric magnitude fields are shown in Fig. 14 with the WAM interpolation. The highest electric force magnitude is observed in the transition region between the Taylor cone and the developed jet, which is roughly 60–70 μm long. This agrees with the classical electrospray theory,[72] which predicts this transition length L_t on the order of 10^1 μm. The electric force vectors are shown in Fig. 15, together with the electric charge density. Similarly to the droplet deformation case, the interpolation method influences the peak charge density and peak electric force magnitude (see Table VIII), increasing from WAM to GM and WHM. This change is not significant enough to disrupt the Taylor cone equilibrium (see Fig. 16) and to influence the jet diameter (see Table VIII). However, it leads to an earlier jet breakup. The average jet length in Table VIII was measured from the electrode orifice exit to the breakup point and was averaged over 500 μs. Jet length variation in time is shown in Fig. 17 for the GM interpolation.

For all three interpolations, the free charge is well contained at the interface, with a minor disruption at the Taylor cone, where the recirculation cell (see Fig. 18) is closest to the interface. Likewise, in the droplet deformation test, the position of the Debye layer moves toward the interface when a sharper interpolation function is selected, resulting in higher peak charge density (see Table VIII).

TABLE VII. Boundary conditions for the EFF case.

Patch	Velocity	Pressure	Phase fraction	Electric Potential	Charge density
Liquid inlet	$\boldsymbol{u} = \boldsymbol{u}_0$	$\partial_n P = 0$	$\alpha = 1$	$\partial_n \phi = 0$	$\partial_n \rho_E = 0$
Capillary	$\boldsymbol{u} = 0$	$\partial_n P = 0$	$\partial_n \alpha = 0$	$\phi = \phi_0$	$\partial_n \rho_E = 0$
Gas inlet	$\partial_n \boldsymbol{u} = 0$	$P = P_0$	$\alpha = 0$	$\partial_n \phi = 0$	$\partial_n \rho_E = 0$
Electrode	$\boldsymbol{u} = 0$	$\partial_n P = 0$	$\partial_n \alpha = 0$	$\phi = 0$	$\partial_n \rho_E = 0$
Atmosphere	$\partial_n \boldsymbol{u} = 0$	$P = 0$	$\partial_n \alpha = 0$	$\partial_n \phi = 0$	$\partial_n \rho_E = 0$
Outlet	$\partial_n \boldsymbol{u} = 0$	$P = 0$	$\partial_n \alpha = 0$	$\phi = 0$	$\partial_n \rho_E = 0$
Axis	Empty[a]				
Front/back	Wedge[b]				

[a]A reduced dimension boundary condition for the axisymmetric case setup.
[b]A boundary condition enforcing cyclic conditions between the two patches.

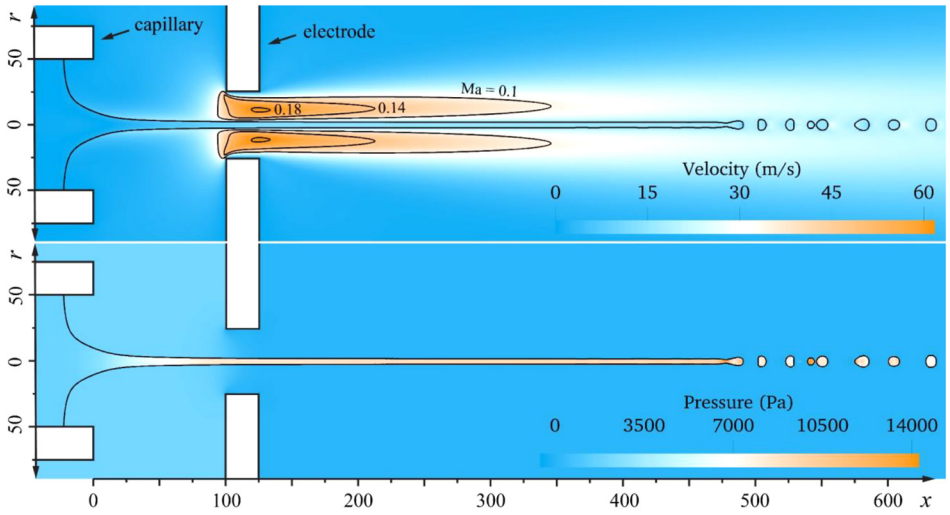

FIG. 13. Velocity (top) and pressure (bottom) field. Mach number contours are drawn in the area of maximum velocity. Radial and axial coordinates are in micrometers.

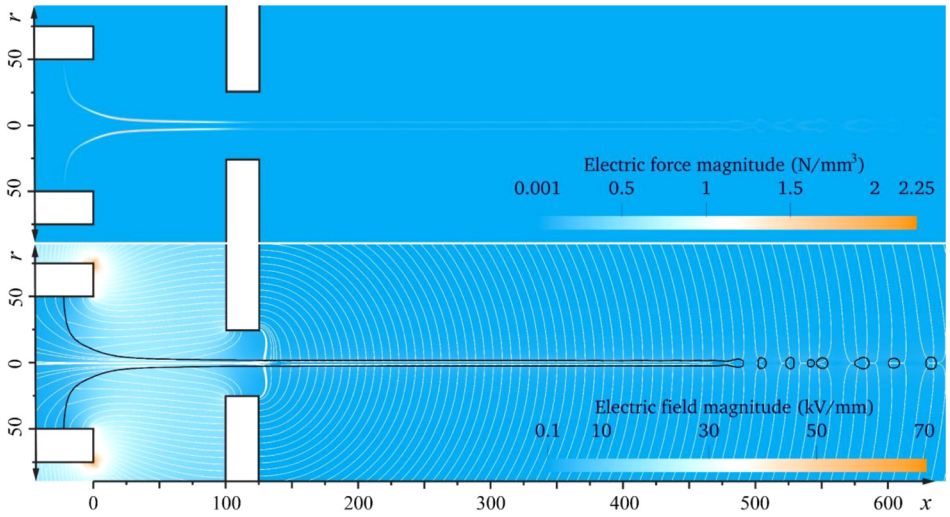

FIG. 14. Electric force magnitude (top) and electric field magnitude with electric field iso-lines (bottom). Radial and axial coordinates are in micrometers.

The jet velocity profile is shown in Fig. 18 (top), and the jet velocity field (bottom). Outside of the electrode, the jet undergoes constant acceleration. We can estimate the acceleration via the material derivative of the velocity $\boldsymbol{a} = \partial_t \boldsymbol{u} + (\boldsymbol{u} \cdot \nabla)\boldsymbol{u}$. We retain only the axial component of the convective term since the jet is radially symmetric and steady in time

$$a(x) = \frac{\boldsymbol{u}^2(x_2) - \boldsymbol{u}^2(x_1)}{2(x_2 - x_1)}. \tag{30}$$

The acceleration is on the order of $10^5\,\mathrm{m\,s^{-2}}$, which is in excellent agreement with the experimental measurements[1,73] of EFF jets.

VII. CONCLUSION

We derived a macroscopic charge conservative EHD numerical model implemented in the FVM-VOF technique from the laws governing the conservation of ionic species based on two assumptions: (i) no ongoing reactions producing ionic species and (ii) fields of relatively high electric potentials where the electric drift of ions is of many orders higher than the thermal stochastic motion. We compared two commonly used approaches to model the electric force source term in the momentum equation and three interpolation methods for the electrical properties of fluids. Two interpolation methods, WAM and WHM, have been readily implemented in the past. In contrast, the GM interpolation is a novelty and was derived as a limit of a previously proposed interpolation[26] for high electrical conductivity ratio EHD problems. The complete set of equations used in the numerical model is collected in Appendix B.

The six models, combining two force and three interpolation methods, were tested against benchmark verification tests with the following conclusions:

(1) All implementations correctly compute the electric field and are charge-conservative. The numerical solution converges toward the analytical solution with mesh refinement.
(2) The pressure jump over the interface due to the electric force is correctly computed using the MSTF approach, while the CPF

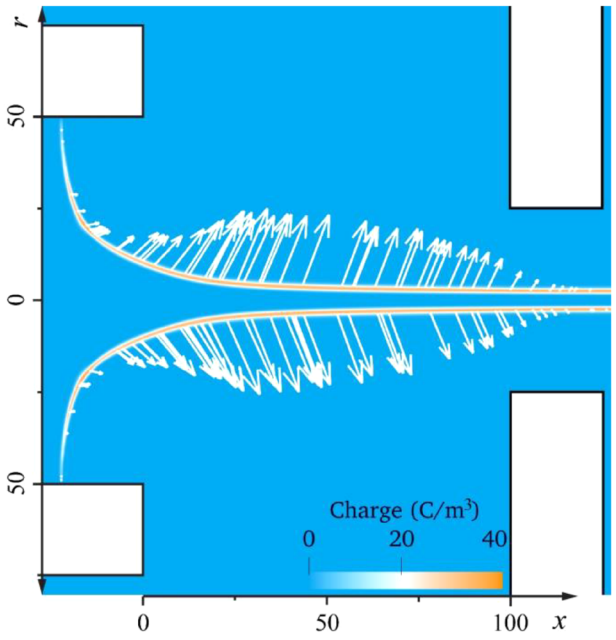

FIG. 15. Volumetric charge density field with electric force vectors at the liquid interface. Radial and axial coordinates are in micrometers.

TABLE VIII. Maximum electric charge density, electric force values, average jet length l and jet diameter d obtained using different interpolation methods. The peak charge density and the electric force values are located at the jet interface in the transition region (see Fig. 15).

	WAM	GM	WHM
$\rho_{E,\max}$ $(\mathrm{C\,m^{-3}})$	39.6	42.2	43.8
$F_{E,\max}$ $(\mathrm{N\,mm^{-3}})$	2.25	2.33	2.42
l_{avg} $(\mu\mathrm{m})$	336.6	315.0	283.3
d_{avg} $(\mu\mathrm{m})$	5.0	5.0	5.0

approach converges to a different value. The absolute difference can be neglected in most practical liquid jet and droplet applications.

(3) The difference in results is below 1% in the WAM, WHM, and GM comparison for all verification tests.

Experimental validation was done against the droplet deformation experiment, with data from Ha and Yang[70] with the following conclusions:

(1) MSTF exhibits prolonged and high-amplitude oscillations during the transient phase of droplet deformation, suggesting less damping and potentially reduced numerical stability.
(2) Furthermore, the MSTF computes substantially different peak charge densities (68% lower) and electric force magnitudes (300% lower) than the CPF. Changes in the interpolation method do not influence the MSTF's result.
(3) The ratio between the initial peak deformation and the steady state deformation is the same for both force implementations.

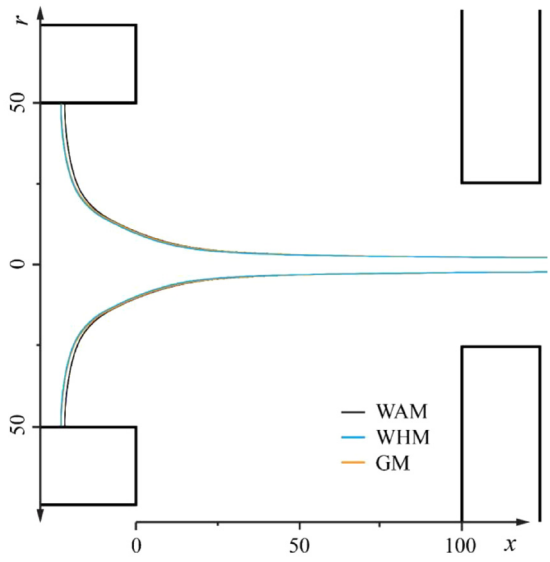

FIG. 16. Meniscus equilibrium shape for WAM, WHM, and GM interpolation functions. Radial and axial coordinates are in micrometers.

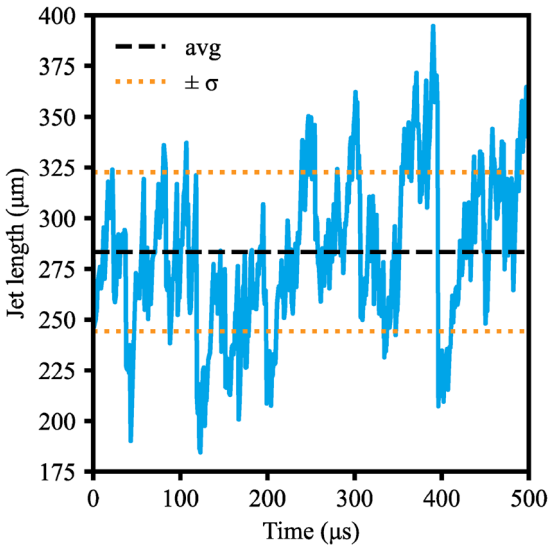

FIG. 17. Jet length as a function of time for the GM case.

Although CPF and MSTF differ in their numerical formulation, they originate from the same physical stress balance. As a result, the normalized transient deformation curves (peak to steady-state ratio) remain consistent across implementations. This suggests that both methods resolve the same dynamical behavior, and differences are primarily in force magnitude scaling due to numerical interpolation and discretization.

(4) CPF depends on the interpolation method, with the sharper functions providing higher peak charge densities, electric forces, and droplet deformations.

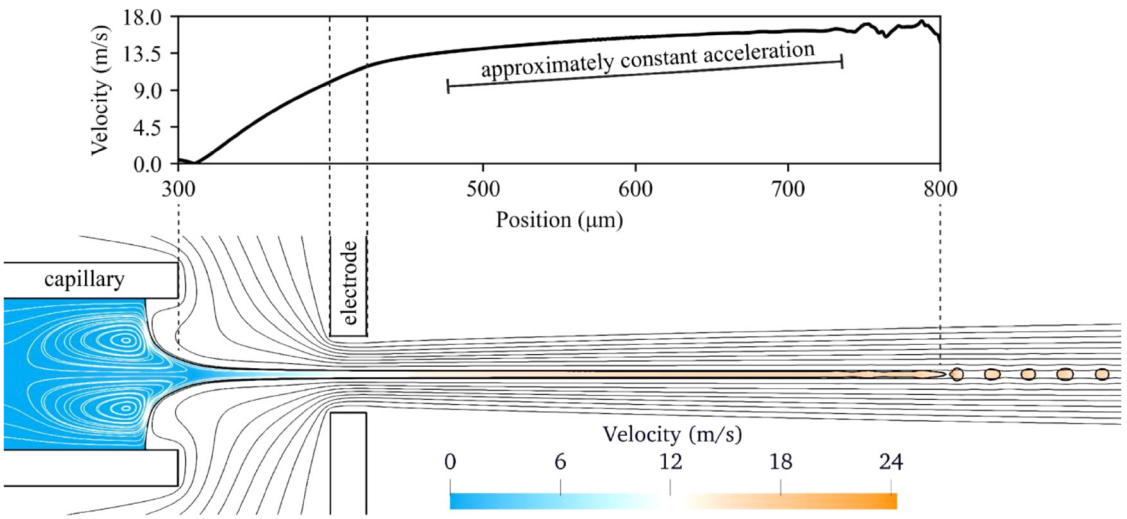

FIG. 18. EFF jet's axial velocity profile from the capillary tip to the jet breakup (top) and the cross section of the jet's velocity field (bottom). The velocity plot and the velocity field are scaled to size.

(5) The CPF-WHM combination is in excellent agreement with the experimental data.
(6) WHM and GM provide a volumetric charge distribution at the interface, which is physically most accurate. WAM computes the charge away from the interface location.

The MSTF implementation shows negligible sensitivity to the interpolation method because it computes the electric force as the divergence of the Maxwell stress tensor, distributing the effect of permittivity and field gradients across neighboring cells in a conservative manner. This approach inherently smooths out variations introduced by different interpolation schemes such as WAM, WHM, or GM, especially within the smeared interface region typical of VOF methods. In contrast, the CPF formulation directly uses local values of electric field and volumetric charge, both of which are highly sensitive to how sharply electrical properties vary across the interface. As a result, CPF captures sharper interfacial forces and deformation changes with different interpolation methods, while MSTF remains largely unaffected due to its global and conservative formulation. It seems that combined with the naturally diffused interface in the VOF method, MSTF tends to underestimate the peak values of both charge and electric force, distributing them more broadly across the interfacial region. Thus, while both methods conserve total force correctly in theory, CPF is better at resolving interfacial peaks, whereas MSTF tends to capture a diffuse average.

To show the robustness of our solver, a simulation of a steady EFF jet is presented. The following conclusions were drawn based on the CPF solver with varying interpolation methods:

(1) Interpolation methods influence jet length but not the jet diameter.
(2) The Taylor cone's shape is influenced by the interpolation method to a small extent, with the GM and WHM methods providing indistinguishable results.
(3) The solver captures the experimentally measured jet velocity profile.
(4) The results are insensitive to the reduction of the electric conductivity of the gas from 10^{-12} to zero.

The WHM interpolation fails for high electric conductivity ratios and dielectric conductivities below $10^{-12}\,\mathrm{S\,m^{-1}}$. GM and WAM can deal with all electrical property ratios.

The reasoning behind the diminished influence of the interpolation method on the EFF jet, which proved substantial in a recent electrospray study,[26] is the following. The change in the peak electric force value was 7% (see Table VIII), which, considering the electric-to-mechanical stress ratio $\chi = 0.72$, increases the overall focusing force by roughly 3%, but is insufficient to deform the jet considerably. However, a slight increase in the electric force does advance the jet's breakup. Thus, when the electric properties are in the WHM working range, we suggest performing numerical simulations using the CPF-WHM solver combination; otherwise, the GM interpolation should be used.

While this study focuses on simplified electrohydrodynamic models that neglect surface charge convection and confinement effects, we acknowledge that these phenomena play a critical role under strong shear, high conductivity contrast, and microscale confinement conditions. Incorporating such effects would require additional interface control equations and introduce significant nonlinear coupling, with implications for numerical stability and model fidelity. Nonetheless, we believe the present results offer a valuable and underexplored reference point for assessing the accuracy and conservation properties of the basic model variants. Our future efforts will extend the presented framework to include surface charge dynamics and confinement effects, aiming to capture the complexities of electrohydrodynamic systems even more comprehensively.

Complementing our focus on model fidelity, we also briefly comment on computational performance. The current implementation shows first-order spatial convergence (see Table V) and scales efficiently for problems ranging from 400k to 2×10^6 cells. The time step cost is only marginally higher than the base VOF solver without

electrostatics, especially after the electric field stabilizes. No clear computational advantage or disadvantage was observed between interpolation methods, including the newly implemented GM scheme. The primary time step limitation arises from the electric relaxation time t_e, which can be significantly shorter than the hydrodynamic time step for conductive fluids. A detailed performance comparison with other methods (e.g., level-set, phase-field) was not included, and we propose this as a direction for future study.

ACKNOWLEDGMENTS

The funding for this research was provided by the Center for Free-Electron Laser Science (CFEL) under the project: Innovative methods for imaging with the use of X-ray free-electron laser (XFEL) and synchrotron sources: simulation of gas-focused micro-jets, and Slovenian Grant and Innovation Agency (ARIS) within Program Group P2-0162 and Project No. J2-4477. This work was also partly supported by the Cluster of Excellence "CUI: Advanced Imaging of Matter" of the Deutsche Forschungsgemeinschaft (DFG)-EXC 2056-project ID390715994. We also acknowledge DESY (Hamburg, Germany), a member of the Helmholtz Association HGF.

AUTHOR DECLARATIONS

Conflict of Interest

The authors have no conflicts to disclose.

Author Contributions

Bor Zupan: Conceptualization (equal); Data Curation (lead); Formal Analysis (lead); Investigation (lead); Software (lead); Visualization (lead); Writing – original draft (lead), Writing – review & editing (equal). **Rizwan Zahoor:** Conceptualization (equal); Software (supporting); Writing – review & editing (equal). **Saša Bajt:** Conceptualization (equal); Funding Acquisition (equal); Writing – review & editing (equal). **Božidar Šarler:** Conceptualization (equal); Funding Acquisition (equal); Supervision (lead)**;** Writing – review & editing (equal).

DATA AVAILABILITY

The data that support the findings of this study are available within the article.

APPENDIX A: DERIVATION OF THE ELECTRIC FORCE

Since the exact derivation of CPF from the divergence of the MST could not be found in the literature by the authors, we provide a complete derivation here, hoping it will serve the readers as a helpful reference. The electric force is calculated from the divergence of the Maxwell stress tensor, which for an electric field $\boldsymbol{E}$ in a medium with permittivity ε is given by

$$\boldsymbol{F}_E = \nabla \cdot \boldsymbol{\tau}_E = \nabla \cdot \left(\varepsilon \boldsymbol{E}\boldsymbol{E} - \frac{1}{2}\varepsilon E^2 \mathrm{I} \right). \tag{A1}$$

Expanding the divergence term

$$\boldsymbol{F}_E = \nabla\varepsilon \cdot (\boldsymbol{E}\boldsymbol{E}) + \varepsilon \nabla \cdot (\boldsymbol{E}\boldsymbol{E}) - \frac{1}{2}\nabla(\varepsilon E^2), \tag{A2}$$

and applying the identity $\nabla \cdot (\boldsymbol{E}\boldsymbol{E}) = \boldsymbol{E} \cdot (\nabla \cdot \boldsymbol{E}) + (\boldsymbol{E} \cdot \nabla)\boldsymbol{E}$, we resolve the first term

$$\boldsymbol{F}_E = \nabla\varepsilon \cdot (\boldsymbol{E}\boldsymbol{E}) + \varepsilon \boldsymbol{E}(\nabla \cdot \mathbf{E}) + \varepsilon(\mathbf{E} \cdot \nabla)\boldsymbol{E} - \frac{1}{2}\nabla(\varepsilon E^2). \tag{A3}$$

Using the product rule, $\nabla(\varepsilon E^2) = (\nabla\varepsilon)E^2 + \varepsilon \cdot \nabla E^2$, and the chain rule $\nabla E^2 = 2\boldsymbol{E} \cdot \nabla \boldsymbol{E}$,

$$\boldsymbol{F}_E = \nabla\varepsilon \cdot (\boldsymbol{E}\boldsymbol{E}) + \varepsilon \boldsymbol{E}(\nabla \cdot \mathbf{E}) + \varepsilon(\mathbf{E} \cdot \nabla)\boldsymbol{E} - \frac{1}{2}E^2\nabla\varepsilon - \varepsilon(\boldsymbol{E} \cdot \nabla)\boldsymbol{E}, \tag{A4}$$

we see that the third and fifth terms on the rhs cancel out, leaving us with

$$\boldsymbol{F}_E = \nabla\varepsilon \cdot (\boldsymbol{E}\boldsymbol{E}) + \varepsilon \boldsymbol{E}(\nabla \cdot \mathbf{E}) - \frac{1}{2}E^2\nabla\varepsilon. \tag{A5}$$

By applying the Gauss law, $\nabla \cdot (\varepsilon \boldsymbol{E}) = \rho_E$, and expanding and rearranging the divergence term, $\varepsilon(\nabla \cdot \boldsymbol{E}) = \rho_E - \nabla\varepsilon \cdot \boldsymbol{E}$, we can expand the second term in (A5)

$$\boldsymbol{F}_E = \nabla\varepsilon \cdot (\boldsymbol{E}\boldsymbol{E}) + \rho_E \boldsymbol{E} - \nabla\varepsilon \cdot (\boldsymbol{E}\boldsymbol{E}) - \frac{1}{2}E^2\nabla\varepsilon, \tag{A6}$$

finally obtaining the sought form

$$\boldsymbol{F}_E = \rho_E \boldsymbol{E} - \frac{1}{2}E^2\nabla\varepsilon. \tag{A7}$$

APPENDIX B: OVERVIEW OF MODELED EQUATIONS

All equations employed in the extended *interFoam* solver are explicitly repeated here for clarity and reproducibility purposes

$$\nabla \cdot (\rho \boldsymbol{u}) = 0, \tag{B1}$$

$$\frac{\partial(\rho \boldsymbol{u})}{\partial t} + \nabla \cdot (\rho \boldsymbol{u}\boldsymbol{u}) = -\nabla P + \nabla \cdot \left[\mu(\nabla \boldsymbol{u} + \nabla \boldsymbol{u}^T) - \frac{2}{3}\mu(\nabla \cdot \boldsymbol{u})\mathbf{I} \right] + \boldsymbol{F}_{ST} + \boldsymbol{F}_E, \tag{B2}$$

$$\nabla \cdot (\varepsilon \boldsymbol{E}) = \rho_E, \tag{B3}$$

$$\frac{\partial \rho_E}{\partial t} + \nabla \cdot (\rho_E \boldsymbol{u}) = -\nabla \cdot (K\boldsymbol{E}), \tag{B4}$$

$$\boldsymbol{F}_E = \nabla \cdot \left(\varepsilon \boldsymbol{E}\boldsymbol{E} - \frac{1}{2}\varepsilon E^2 \mathrm{I} \right), \tag{B5}$$

$$\boldsymbol{F}_E = \rho_E \boldsymbol{E} - \frac{1}{2}\boldsymbol{E}^2\nabla\varepsilon, \tag{B6}$$

$$\Psi = \Psi_1\alpha_1 + \Psi_2\alpha_2, \tag{B7}$$

$$\Psi = \left(\frac{\alpha_1}{\Psi_1} + \frac{\alpha_2}{\Psi_2} \right)^{-1}, \tag{B8}$$

$$\Psi = \Psi_1^{\alpha_1}\Psi_2^{\alpha_2}. \tag{B9}$$

REFERENCES

[1]B. Zupan *et al.*, "An experimental study of liquid micro-jets produced with a gas dynamic virtual nozzle under the influence of an electric field," Front. Mol. Biosci. **10**, 1006733 (2023).

[2]F. Cruz-Mazo *et al.*, "Aerodynamically stabilized Taylor cone jets," Phys. Rev. E **100**, 031101 (2019).
[3]T. R. M. Barends, B. Stauch, V. Cherezov, and I. Schlichting, "Serial femtosecond crystallography," Nat. Rev. Methods Primers **2**, 59 (2022).
[4]A. Thuppul, P. L. Wright, A. L. Collins, J. K. Ziemer, and R. E. Wirz, "Lifetime considerations for electrospray thrusters," Aerospace **7**, 108 (2020).
[5]J. M. Montanero and A. M. Gañán-Calvo, "Dripping, jetting and tip streaming," Rep. Prog. Phys. **83**, 097001 (2020).
[6]J. M. López-Herrera, S. Popinet, and M. A. Herrada, "A charge-conservative approach for simulating electrohydrodynamic two-phase flows using volume-of-fluid," J. Comput. Phys. **230**, 1939–1955 (2011).
[7]R. Zahoor, G. Belšak, S. Bajt, and B. Šarler, "Simulation of liquid micro-jet in free expanding high-speed co-flowing gas streams," Microfluid. Nanofluid. **22**, 87 (2018).
[8]G. I. Taylor, "Studies in electrohydrodynamics. I. The circulation produced in a drop by an electric field," Proc. R. Soc. London, Ser. A **291**, 159–166 (1966).
[9]H. J. Cho, I. S. Kang, Y. C. Kweon, and M. H. Kim, "Study of the behavior of a bubble attached to a wall in a uniform electric field," Int. J. Multiphase Flow **22**, 909–922 (1996).
[10]H. J. Cho, I. S. Kang, Y. C. Kweon, and M. H. Kim, "Numerical study of the behavior of a bubble attached to a tip in a nonuniform electric field," Int. J. Multiphase Flow **24**, 479–498 (1998).
[11]J. C. Baygents, N. J. Rivette, and H. A. Stone, "Electrohydrodynamic deformation and interaction of drop pairs," J. Fluid Mech. **368**, 359–375 (1998).
[12]F. J. Higuera, "Injection of bubbles in a quiescent inviscid liquid under a uniform electric field," J. Fluid Mech. **568**, 203–222 (2006).
[13]J. D. Sherwood, "Breakup of fluid droplets in electric and magnetic fields," J. Fluid Mech. **188**, 133–146 (1988).
[14]P. K. Notz and O. A. Basaran, "Dynamics of drop formation in an electric field," J. Colloid Interface Sci. **213**, 218–237 (1999).
[15]M. T. Harris and O. A. Basaran, "Equilibrium shapes and stability of nonconducting pendant drops surrounded by a conducting fluid in an electric field," J. Colloid Interface Sci. **170**, 308–319 (1995).
[16]M. T. Harris and O. A. Basaran, "Capillary electrohydrostatics of conducting drops hanging from a nozzle in an electric field," J. Colloid Interface Sci. **161**, 389–413 (1993).
[17]O. A. Basaran and L. E. Scriven, "Axisymmetric shapes and stability of pendant and sessile drops in an electric field," J. Colloid Interface Sci. **140**, 10–30 (1990).
[18]J. Zhang and D. Y. Kwok, "A 2D lattice Boltzmann study on electrohydrodynamic drop deformation with the leaky dielectric theory," J. Comput. Phys. **206**, 150–161 (2005).
[19]N. Talat *et al.*, "Development of meshless phase field method for two-phase flow," Int. J. Multiphase Flow **108**, 169–180 (2018).
[20]J. M. López-Herrera, M. A. Herrada, and A. M. Gañán-Calvo, "Electrokinetic modelling of cone-jet electrosprays," J. Fluid Mech. **964**, A19 (2023).
[21]J. C. Baygents and D. A. Saville, "The circulation produced in a drop by an electric field: A high field strength electrokinetic model," AIP Conf. Proc. **197**, 7–17 (1990).
[22]E. K. Zholkovskij, J. H. Masliyah, and J. Czarnecki, "An electrokinetic model of drop deformation in an electric field," J. Fluid Mech. **472**, 1–27 (2002).
[23]O. Schnitzer and E. Yariv, "The Taylor–Melcher leaky dielectric model as a macroscale electrokinetic description," J. Fluid Mech. **773**, 1–33 (2015).
[24]Y. Mori and Y.-N. Young, "From electrodiffusion theory to the electrohydrodynamics of leaky dielectrics through the weak electrolyte limit," J. Fluid Mech. **855**, 67–130 (2018).
[25]G. Tomar *et al.*, "Two-phase electrohydrodynamic simulations using a volume-of-fluid approach," J. Comput. Phys. **227**, 1267–1285 (2007).
[26]H. Huh and R. E. Wirz, "Simulation of electrospray emission processes for low to moderate conductivity liquids," Phys. Fluids **34**, 112017 (2022).
[27]A. M. Gañán-Calvo, J. M. López-Herrera, M. A. Herrada, A. Ramos, and J. M. Montanero, "Review on the physics of electrospray: From electrokinetics to the operating conditions of single and coaxial Taylor cone-jets, and AC electrospray," J. Aerosol Sci. **125**, 32–56 (2018).
[28]Q. Yang, Z. Wang, Q. Gao, Y. Zhao, and C. Jiang, "Study of droplet formation in parallel flow focusing microchannel under electrostatic field control," Colloids Surf., A **695**, 134174 (2024).
[29]L. Li and C. Zhang, "Electro-hydrodynamics of droplet generation in a co-flowing microfluidic device under electric control," Colloids Surf., A **586**, 124258 (2020).
[30]D. Wang, L. Chagot, J. Wang, and P. Angeli, "Effect of electric field on droplet formation in a co-flow microchannel," Phys. Fluids **37**, 023331 (2025).
[31]R. Zahoor, J. Knoška, S. Bajt, and B. Šarler, "Experimental and numerical investigation of gas-focused liquid micro-jet velocity," Int. J. Multiphase Flow **135**, 103530 (2021).
[32]K. Kovačič, J. Gregorc, and B. Šarler, "Numerical modelling and experimental validation of dripping, jetting and whipping modes of gas dynamic virtual nozzle," Int. J. Numer. Methods Heat Fluid Flow **34**, 1582–1608 (2024).
[33]K. Kovačič and B. Šarler, "The kinetic energy transfer analysis between the gas and the liquid in flow-focusing of the micro-jet," J. Phys.: Conf. Ser. **2766**, 012075 (2024).
[34]E. R. Williams, "The global electrical circuit: A review," Atmos. Res. **91**, 140–152 (2009).
[35]K. Kovačič, S. Bajt, and B. Šarler, "Numerical analysis of Knudsen number of helium flow through gas-focused liquid sheet micro-nozzle," Fluids **9**, 273 (2024).
[36]H. Dastourani, M. R. Jahannama, and A. Eslami-Majd, "A physical insight into electrospray process in cone-jet mode: Role of operating parameters," Int. J. Heat Fluid Flow **70**, 315–335 (2018).
[37]O. Lastow and W. Balachandran, "Numerical simulation of electrohydrodynamic (EHD) atomization," J. Electrost. **64**, 850–859 (2006).
[38]H. Paknemat, A. R. Pishevar, and P. Pournaderi, "Numerical simulation of drop deformations and breakup modes caused by direct current electric fields," Phys. Fluids **24**, 102101 (2012).
[39]M. A. Herrada *et al.*, "Numerical simulation of electrospray in the cone-jet mode," Phys. Rev. E **86**, 026305 (2012).
[40]J. D. Berry, M. R. Davidson, and D. J. E. Harvie, "A multiphase electrokinetic flow model for electrolytes with liquid/liquid interfaces," J. Comput. Phys. **251**, 209–222 (2013).
[41]C. Ferrera, J. M. López-Herrera, M. A. Herrada, J. M. Montanero, and A. J. Acero, "Dynamical behavior of electrified pendant drops," Phys. Fluids **25**, 012104 (2013).
[42]M. Forget and M. Jugroot, "Electrohydrodynamic modeling of electrospray cone-jets for spacecraft propulsion," in *Proceedings of the 33rd International Electric Propulsion Conference* (The George Washington University, Washington, D.C., 2013).
[43]A. Najjaran, R. Ebrahimi, M. Rahmanpoor, and A. Najjaran, "Numerical simulation of electrohydrodynamic (EHD) atomization in the cone-jet mode," Appl. Mech. Mater. **325–326**, 180–185 (2013).
[44]I. Roghair, D. Van Den Ende, and F. Mugele, "An OpenFOAM-based electrohydrodynamic model," in Proceedings of the 8th International Conference on Multiphase Flow, Jeju, South Korea, 2013.
[45]N. C. Lima and M. A. d'Ávila, "Numerical simulation of electrohydrodynamic flows of Newtonian and viscoelastic droplets," J. Non-Newtonian Fluid Mech. **213**, 1–14 (2014).
[46]X. Chen, Y. Song, D. Li, and G. Hu, "Deformation and interaction of droplet pairs in a microchannel under ac electric fields," Phys. Rev. Appl. **4**, 024005 (2015).
[47]J. M. López-Herrera, A. M. Gañán-Calvo, S. Popinet, and M. A. Herrada, "Electrokinetic effects in the breakup of electrified jets: A volume-of-fluid numerical study," Int. J. Multiphase Flow **71**, 14–22 (2015).
[48]I. Roghair *et al.*, "A numerical technique to simulate display pixels based on electrowetting," Microfluid. Nanofluid. **19**, 465–482 (2015).
[49]M. Rahmanpour and R. Ebrahimi, "Numerical simulation of electrohydrodynamic spray with stable Taylor cone–jet," Heat Mass Transfer **52**, 1595–1603 (2016).
[50]H. Dastourani, M. R. Jahannama, and A. Eslami Majd, "Numerical simulation of drop deformation and breakup in an electric field," Amirkabir J., Mech. Eng. **50**(4), 767–784 (2018).
[51]X. Huang *et al.*, "Breakup mode transformation of leaky dielectric droplet under direct current electric field," Int. J. Multiphase Flow **96**, 123–133 (2017).
[52]M. Rahmanpour, "Numerical simulation of highly charged droplets dynamics with primary break-up in electrospray at sub Rayleigh limit," J. Appl. Fluid Mech. **10**, 541–550 (2017).

[53]M. Rahmanpour, R. Ebrahimi, and A. Pourrajabian, "Numerical simulation of two-phase electrohydrodynamic of stable Taylor cone–jet using a volume-of-fluid approach," J. Braz. Soc. Mech. Sci. Eng. **39**, 4443–4453 (2017).
[54]M. Wu, P. M. Sammons, and K. Barton, "Numerical modeling of high resolution electrohydrodynamic jet printing using OpenFOAM," in 2017 Proceedings of 28th Annual International Solid Freeform Fabrication Symposium – Additive Manufacturing Conference, 2017.
[55]E. Ghasemi, H. Bararnia, S. Soleimanikutanaei, and C. X. Lin, "Simulation of deformation and fragmentation of a falling drop under electric field," Powder Technol. **325**, 301–308 (2018).
[56]L. Guo *et al.*, "Charged satellite drop avoidance in electrohydrodynamic dripping," Micromachines **10**, 172 (2019).
[57]H. Huh and R. E. Wirz, "Numerical simulation of electrospray thruster extraction," in Proceedings of the 36th International Electric Propulsion Conference, Vienna, Austria, 2019.
[58]Y. Pan and L. Zeng, "Simulation and validation of droplet generation process for revealing three design constraints in electrohydrodynamic jet printing," Micromachines **10**, 94 (2019).
[59]Z. Jiang, Y. Gan, and Y. Shi, "An improved model for prediction of the cone-jet formation in electrospray with the effect of space charge," J. Aerosol Sci. **139**, 105463 (2020).
[60]K. C. Sahu, M. K. Tripathi, J. Chaudhari, and S. Chakraborty, "Simulations of a weakly conducting droplet under the influence of an alternating electric field," Electrophoresis **41**, 1953–1960 (2020).
[61]H. Huh and R. E. Wirz, "Numerical simulation of cone-jet and emission processes for electrospray thrusters," in *Proceedings of the 37th International Electric Propulsion Conference* (MIT, MA, 2022).
[62]J. Q. Feng, "Electrohydrodynamic behaviour of a drop subjected to a steady uniform electric field at finite electric Reynolds number," Proc. R. Soc. London, Ser. A **455**, 2245–2269 (1999).
[63]P. Sheehy and M. Owkes, "Numerical study of electric Reynolds number on electrohydrodynamic (EHD) assisted atomization," Atomization Sprays **27**, 645–664 (2017).
[64]F. Moukalled, L. Mangani, and M. Darwish, "The finite volume method," in *The Finite Volume Method in Computational Fluid Dynamics: An Advanced Introduction with OpenFOAM® and Matlab*, edited by F. Moukalled, L. Mangani, and M. Darwish (Springer International Publishing, Cham, 2016), pp. 103–135.
[65]C. W. Hirt and B. D. Nichols, "Volume of fluid (VOF) method for the dynamics of free boundaries," J. Comput. Phys. **39**, 201–225 (1981).
[66]J. U. Brackbill, D. B. Kothe, and C. Zemach, "A continuum method for modeling surface tension," J. Comput. Phys. **100**, 335–354 (1992).
[67]H. G. Weller, G. Tabor, H. Jasak, and C. Fureby, "A tensorial approach to computational continuum mechanics using object-oriented techniques," Comput. Phys. **12**, 620–631 (1998).
[68]S. W. J. Welch and G. Biswas, "Direct simulation of film boiling including electrohydrodynamic forces," Phys. Fluids **19**, 012106 (2007).
[69]O. O. Ajayi, "A note on Taylor's electrohydrodynamic theory," Proc. R. Soc. London, Ser. A **364**, 499–507 (1978).
[70]J.-W. Ha and S.-M. Yang, "Deformation and breakup of Newtonian and non-Newtonian conducting drops in an electric field," J. Fluid Mech. **405**, 131–156 (2000).
[71]J. R. Karp, B. Lecordier, and M. S. Shadloo, "Electrohydrodynamic flows inside a neutrally buoyant leaky dielectric drop," Phys. Fluids **36**, 053323 (2024).
[72]A. M. Gañán-Calvo, J. M. López-Herrera, and P. Riesco-Chueca, "The combination of electrospray and flow focusing," J. Fluid Mech. **566**, 421 (2006).
[73]B. Zupan, S. Bajt, H. N. Chapman, and B. Šarler, "Acceleration of flow-focused liquid jets in the presence of a strong electric field," J. Phys.: Conf. Ser. **2766**, 012070 (2024).